Check for updates

AGU ADVANCING EARTH AND SPACE SCIENCES

Water Resources Research

RESEARCH ARTICLE
10.1029/2023WR035334

A Novel Local-Inertial Formulation Representing Subgrid Scale Topographic Effects for Urban Flood Simulation

N. Nithila Devi[1,2] **and Soumendra Nath Kuiry**[2]

[1]Section Hydrology, GFZ German Research Centre for Geoscience, Potsdam, Germany, [2]Hydraulic and Water Resources Engineering Division, Department of Civil Engineering, Indian Institute of Technology Madras, Chennai, India

Key Points:

- A subgrid-based local-inertial formulation that makes computations at coarse grids while capturing the within-grid terrain is proposed
- It is faster than a full 2D model and can resolve complex urban terrain (streets, canals, roads) where existing coarse grid models fail
- It improves mass flux estimation of coarse grids and holds promise in real-time forecasting of slow-rising urban floods

Supporting Information:

Supporting Information may be found in the online version of this article.

Correspondence to:

S. N. Kuiry,
snkuiry@civil.iitm.ac.in

Citation:

Nithila Devi, N., & Kuiry, S. N. (2024). A novel local-inertial formulation representing subgrid scale topographic effects for urban flood simulation. *Water Resources Research*, *60*, e2023WR035334. https://doi.org/10.1029/2023WR035334

Received 27 MAY 2023
Accepted 3 APR 2024

Author Contributions:

Conceptualization: N. Nithila Devi, Soumendra Nath Kuiry
Data curation: Soumendra Nath Kuiry
Formal analysis: N. Nithila Devi
Investigation: N. Nithila Devi, Soumendra Nath Kuiry
Methodology: N. Nithila Devi, Soumendra Nath Kuiry
Project administration: Soumendra Nath Kuiry
Resources: Soumendra Nath Kuiry
Software: N. Nithila Devi
Supervision: Soumendra Nath Kuiry
Validation: N. Nithila Devi
Visualization: N. Nithila Devi
Writing – original draft: N. Nithila Devi

© 2024. The Authors.
This is an open access article under the terms of the Creative Commons Attribution License, which permits use, distribution and reproduction in any medium, provided the original work is properly cited.

Abstract The local-inertial approximations of the shallow water equations (SWEs) have been used for flood forecasting at larger spatial scales owing to the improved computational efficiency and similar accuracy compared to the full 2D SWEs. With the availability of high-resolution elevation data, the complex terrain of urban areas with various small-scale features is represented well. Even for a local-inertial model, utilizing such high-resolution elevation data in flood simulations of urbanized areas increases the computational cost. A subgrid-based local-inertial formulation that permits large numerical grid size for computations while preserving the within-grid topography is proposed to circumvent this. The subgrid topography can be incorporated into the coarse numerical grid computations by estimating the hydraulic properties, namely, volume and face area, based on water surface elevation variations of the associated high-resolution terrain. The pre-stored hydraulic properties are then used to dynamically update the hydraulic variables during the execution of the local-inertial model. Idealized and real-world test cases were simulated to illustrate the advantages of the proposed model. The proposed subgrid model performs better in capturing flood depth around subgrid-scale features such as streets, highways, minor canals, etc., than the simple grid-averaged local-inertial models of the same grid size. The proposed model is faster than the existing local-inertial model (e.g., LISFLOOD-FP) (~21–34 times) and the full 2D model (e.g., HEC-RAS 2D) (~361–660 times) of similar accuracy in the slow-rising flood applications. Thus, the subgrid local-inertial model holds promise in real-time flood inundation forecasting, resolving smaller urban features.

Plain Language Summary Quick and accurate flood forecasting is crucial in highly populated urban areas with several small terrain features like roads, streets, highways, canals, etc. The simulation of flood depth and extent can be made faster by using simplified equations or dividing the domain into larger grids. The equations will be solved over each grid, generating flood depth and flow. However, opting for a large grid will not capture smaller within-grid terrain elements. Therefore, this paper proposes a novel subgrid-based local-inertial model that uses simplified equations and operates at a large grid while still representing the within-grid terrain. The subgrid-inertial model simulates flooding around the smaller features of urban areas with less time than finer grid full 2D models. Meanwhile, the existing local-inertial models operating at large grids often fail to resolve urban terrain features. Thus, using limited computing facilities, the proposed subgrid-inertial model is highly suited for real-time riverine flood forecasting in urbanized floodplains.

1. Introduction

Globally, increasing impermeable surfaces due to urban expansion and extreme precipitation exacerbate the flood risk (Wasko & Sharma, 2015; Wuebbles et al., 2017). Therefore, reliable and time-efficient simulation of floods are quintessential in (a) flood forecasting from basin to national and global scales (Neal, Schumann, & Bates, 2012; Pappenberger, Beven, Horritt, & Blazkova, 2005; Pappenberger, Beven, Hunter, et al., 2005; Robson et al., 2016; Thielen et al., 2009; Yamazaki et al., 2013); (b) ensemble or probabilistic flood inundation forecasting (Ahmadisharaf & Kalyanapu, 2019; Barthélémy et al., 2017; Cloke & Pappenberger, 2009; Pappenberger, Beven, Horritt, & Blazkova, 2005; Pappenberger, Beven, Hunter, et al., 2005; W. Wu et al., 2020); (c) sensitivity and predictive uncertainty analysis (Aronica et al., 2002; Aronica et al., 2012; Bhuyian et al., 2015; Di Baldassarre et al., 2010; Merwade et al., 2008; Pappenberger, Beven, Horritt, & Blazkova, 2005; Pappenberger, Beven, Hunter, et al., 2005; Smemoe et al., 2007; Stephens & Bledsoe, 2020; Try et al., 2018); and (d) optimization trials of flood management alternatives involving probabilistic multi-criteria decision making (Ahmadisharaf et al., 2016). The disaster mitigation and management authorities rely on accurate urban flood forecasting to save lives and properties. With the advent of the latest technologies like LiDAR and structure-from-motion (sfm)

Writing – review & editing: N. Nithila Devi, Soumendra Nath Kuiry

photogrammetry, the complex terrain of the urban landscape is being represented through high-resolution elevation data sets (Casas et al., 2012; Meesuk et al., 2015; Smeeckaert et al., 2013; Wang & Philpot, 2007). In that light, the terrain features that influence the flow dynamics need to be included in the hydraulic models by resorting to smaller grid sizes (Bates et al., 2003; Brown et al., 2007; Fewtrell et al., 2008; Horritt & Bates, 2001; Horritt et al., 2010; Neal, Bates, et al., 2009; Neal, Fewtrell, & Trigg, 2009; Sampson et al., 2012). Though the accuracy of urban flood simulation is improved, the computational cost is compounded. Even with the recent advances, it is still challenging to run hydraulic simulations without resorting to supercomputing facilities (Dottori et al., 2013; Hodges, 2015; Neal et al., 2010; Neal, Bates, et al., 2009; Neal, Fewtrell, & Trigg, 2009; Schubert et al., 2022). The challenge to balance computational efficiency and accuracy is further amplified in large areas, extended period and/or Monte Carlo simulations.

On the other hand, when the grid sizes are coarsened, many instances of the hydraulic model can be run on desktop workstations without resorting to high-end computational infrastructure (F. Dottori et al., 2013; Hodges, 2015). Added to that, opting for a fine-resolution mesh requires complex parameterization of the hydraulic model, especially in flow resistance (Chen et al., 2012a; Dottori et al., 2013; Guinot, 2012; Sanders et al., 2008; Soares-Frazão et al., 2008). Notably, the choice of grid size for two-dimensional (2D) models needs to be done with caution, especially in real-time flood forecasting systems and other earlier-mentioned scenarios, where the model run time is a critical factor (Dottori et al., 2013). The need for using rainfall ensemble nowcasts and short-range forecasts to reduce uncertainty and generate sufficient lead time for the decision-makers involved in flood management makes it even more of a herculean task (Ivanov et al., 2021; Schubert et al., 2022). Thus, a lot of research and practical gaps exist in real-time operational flood forecasting at high-resolution, especially in urban areas (Chen et al., 2012a; Fernández-Pato & García-Navarro, 2016; Ivanov et al., 2021; Jordi et al., 2019; Leandro et al., 2009; Leitão et al., 2010; Liang et al., 2015; Ming et al., 2020; Sanders et al., 2010; Sanders & Schubert, 2019; Schubert et al., 2022; Su et al., 2019; Wing et al., 2019; Zhao et al., 2019).

Some of the alternative ways to reduce the computation cost while still making use of high-resolution data include employing (a) simplified hydraulic models like diffusive (Yamazaki et al., 2011, 2012) or local-inertial (Bates et al., 2010; De Almeida et al., 2012; Sridharan et al., 2020, 2021; Yamazaki et al., 2013) formulations of the Shallow Water Equations (SWEs), cellular automata models, etc. (Dottori & Todini, 2010; Guidolin et al., 2016; Liu & Pender, 2013); (b) high performing computer architectures utilizing parallel processing such as cloud-based computing (Lamb et al., 2009), graphical processing units (Kalyanapu et al., 2011), multi-core central processing units (MCs); distributed memory parallelization (Apel et al., 2022; Neal, Bates, et al., 2009; Neal, Fewtrell, & Trigg, 2009; Pau & Sanders, 2006; Sanders & Schubert, 2019), and (c) subgrid treatment approaches that represent high-resolution topography within the grids (Casulli, 2009; Defina, 2000; Guinot, 2017b; Li & Hodges, 2019; McMillan & Brasington, 2007; Sanders et al., 2008; Stelling, 2012; Volp et al., 2013; G. Wu et al., 2016).

Considering the simplified models, local-inertial formulation neglects the convective acceleration terms and allows for large stable time steps in considerable water depth and small surface slope areas than the diffusive models (Bates et al., 2010; Hunter et al., 2006; Sridharan et al., 2020, 2021). The local-inertial models offer a more realistic representation of flood hydrodynamics and are faster than the diffusive models. Also, it was reported by Dazzi et al. (2021) that when the grid size was coarser, both local-inertial and full 2D models performed similarly with respect to the inundation extent, water levels and flood arrival times. It was also shown that the convective acceleration was negligible at coarser grid size, even for the Secchia levee-breach-inundation case study, where the flow was briefly supercritical in a spatially limited region. It is important to mention that the local-inertial models may not function similarly to the full 2D SWE models in regions of flow transitions, hydraulic jumps and shocks. When the flow conditions are near to supercritical or flash flood conditions, the local-inertial approximation underestimates the velocities (De Almeida & Bates, 2013) and therefore, the simulations can be considered as low-boundary estimations (Shaw et al., 2021). Nevertheless, the local-inertial models function similarly to the full 2D SWE models in areas where the shocks are absent, and the flow regime is subcritical (De Almeida et al., 2012). The applicability of the local-inertial models for subcritical, slow-rising floods during excessive rainfall has been confidently established in several studies (Apel et al., 2022; Dazzi et al., 2021; De Almeida et al., 2012; Lewis et al., 2013; Neal, Villanueva, et al., 2012; Ozdemir & Akbas, 2023; Sanyal et al., 2013; Shustikova et al., 2019; Sridharan et al., 2020, 2021; Yamazaki et al., 2013). The local-inertial models have attracted many researchers in the past decade (Bates et al., 2010; Coulthard et al., 2013; Courty et al., 2017; Dottori et al., 2016; Pontes et al., 2017; Sridharan et al., 2020; Yamazaki et al., 2013) mainly due to

19447973, 2024, 5, Downloaded from https://agupubs.onlinelibrary.wiley.com/doi/10.1029/2023WR035334 by Helmholtz-Zentrum Potsdam GFZ, Wiley Online Library on [14/05/2024]. See the Terms and Conditions (https://onlinelibrary.wiley.com/terms-and-conditions) on Wiley Online Library for rules of use; OA articles are governed by the applicable Creative Commons License

19447973, 2024, 5, Downloaded from https://agupubs.onlinelibrary.wiley.com/doi/10.1029/2023WR035334 by Helmholtz-Zentrum Potsdam GFZ, Wiley Online Library on [14/05/2024]. See the Terms and Conditions (https://onlinelibrary.wiley.com/terms-and-conditions) on Wiley Online Library for rules of use; OA articles are governed by the applicable Creative Commons License

their low computational cost, which is a crucial factor in formulating emergency action plans for saving lives and properties from flood damages. In that regard, the local-inertial formulations are employed both as stand-alone hydraulic models (e.g., LISFLOOD-FP by Bates et al., 2010) and coupled with hydrologic and landscape evolution models, namely, CaMa-Flood (Yamazaki et al., 2013), Itzï (Courty et al., 2017), CAESAR-LISFLOOD (Coulthard et al., 2013) and MGB-IPH (De Paiva et al., 2013; Pontes et al., 2017). The simplified local-inertial models have been used for large-scale flood mapping owing to the computational advantage as shown in the studies of Devitt et al. (2023), Falter et al. (2013), Neal, Schumann, and Bates (2012), Savage et al. (2016), Wing et al. (2017), and Sridharan et al. (2020). Specifically, regarding the application to urban areas, several studies (Apel et al., 2022; Ozdemir & Akbas, 2023; Shustikova et al., 2019; Sridharan et al., 2020, 2021) have reported the successful implementation of the local-inertial models in the case of slow-rising floods. Apart from validation with observed data, some studies have bench-marked them with full-2D models like HEC-RAS, MIKE and TELEMAC (Shustikova et al., 2019; Sridharan et al., 2020, 2021). These studies establish that simulations from local-inertial models have an accuracy comparable to full 2D models with notable computational advantage for subcritical flows.

Regarding the subgrid approaches, the porosity-based shallow water models are often examined, and it was found that the computational cost gets reduced by two or three orders of magnitude (Guinot, 2017b). The porosity that represents the fraction occupied by voids is treated as a function of water surface elevation and is multiplied into the SWEs of coarse grids, allowing the within-grid high-resolution topography to be included in the computations. As proposed by Defina et al. (1994), in the earlier approaches, only a single porosity was used in the SWEs (Benkhaldoun et al., 2016; Cea & Vázquez-Cendón, 2010; Defina, 2000; Guinot & Soares-Frazão, 2006; Petaccia et al., 2009; Soares-Frazão et al., 2008; Velickovic et al., 2017; Viero & Valipour, 2017; Yu & Lane, 2006). McMillan and Brasington (2007) included porosity in continuity and kinematic momentum equations, and it was reported that the coarser model's performance was sensitive to roughness values. Later, in order to address the inherent anisotropy of the urban areas with their complex terrain composed of asymmetric buildings and different alignments of the streets governing the flow dynamics, two types of porosities (storage porosity for continuity and connection porosity for momentum equations) were embedded into the integral form of equations (Guinot, 2012, 2017a; Guinot et al., 2017; Özgen et al., 2016; Sanders et al., 2008; G. Wu et al., 2016). Chen et al. (2012a) introduced building coverage ratio (BCR) and conveyance reduction factor (CRF) in the 2D non-inertial SWEs, and it worked for buildings bisecting the coarse cell. Chen et al. (2012b) proposed a multi-layer approach that generates different layers for the coarse cells with buildings defining individual flow paths. Each layer would have different BCR and CRF values to mimic the flow paths in and around the buildings within the coarse cell, using cellular automata. Though the model worked successfully for synthetic and smaller test cases, generating layers for urban layouts with more than thousands of buildings was a demanding task. Later, Guinot (2017b) demonstrated, using a simple idealized urban layout, that the models with two types of porosities are sensitive to the grid design. Guinot (2017b) also concluded that if a rectangular grid was used, then the cell edges should be aligned with the street network's principal direction to avoid altering the magnitude and direction of the wave propagation. The need to fine-tune the edge/connectivity porosity apart from the urban geometry to ensure continuous solution was also underscored. However, there are practical implications in adjusting the edge porosity of two cells sharing a common interface, as the adjustments may propagate from one cell to the other. Bruwier et al. (2017) concluded that using different porosity parameters for each term in SWE can reduce the error in flooded depth estimates. The study also acknowledges that the transfer of such a methodology to more complex geometries is highly cumbersome and is applicable only to simple urban configurations. Viero (2019) implemented subgrid porosity within a finite element framework to solve the full 2D SWEs. In particular, the conveyance porosity is represented using a tensor formulation, as the impact of buildings may not be reflected in the two primary directions alone. This model was tested for urban layouts that were almost homogeneous. The study points out the challenge of characterizing the conveyance porosity for real cases from both geometric and hydraulic perspectives. Ferrari et al. (2019) solved isotropic storage porosity-based SWEs and used anisotropic conveyance porosity to express friction source term in tensor form to reduce mesh sensitivity. This study, therefore, highlights the need to test the ways of defining the porosities in real complex urban networks, which are, therefore, still in the early stages of development.

Casulli (2009) proposed a porosity-depth coupled approach to solve SWEs to account for within-grid complexity while ensuring mass conservation. This approach integrates the known within-grid bathymetry over the computational cells and edges, and the momentum equation is substituted into the continuity equation. As the

19447973, 2024, 5, Downloaded from https://agupubs.onlinelibrary.wiley.com/doi/10.1029/2023WR035334 by Helmholtz-Zentrum Potsdam GFZ, Wiley Online Library on [14/05/2024]. See the Terms and Conditions (https://onlinelibrary.wiley.com/terms-and-conditions) on Wiley Online Library for rules of use; OA articles are governed by the applicable Creative Commons License

volume is expressed in terms of the free surface elevation, the coupled approach results in a non-linear equation for the free surface, and therefore, it differs from the conventional porosity methods (Platzek et al., 2016). The porosity-depth coupled approach provides accurate wetting and drying representation and allows for flow in within-grid channels without resorting to grid refinement (Casulli, 2009; Casulli & Stelling, 2011). This approach has successfully improved the model performance in Elbe River sections (Platzek et al., 2016; Sehili et al., 2014). Sehili et al. (2014) showed a speed-up of 25 times when the porosity-depth coupled approach was implemented for a hindcast in the Elbe estuary. Li and Hodges (2019) also implemented the porosity-depth approach by pre-storing the relationships between subgrid variables (face area and volume) and water surface elevation and using them directly in the SWEs while solving them on a coarser grid. The model was used to simulate hydrodynamics and salinity in shallow coastal areas of the Nueces Delta. It has been shown that their model can give results close to fine-grid simulation in terms of water surface elevation, inundation area, flow rate and salinity with less computational time.

Another approach to grid coarsening is grid nesting techniques in certain areas of the domain. Nevertheless, these methods require the modeler to make correct judgments in defining the areas for grid refinement with structures that may chiefly alter the flow dynamics (Hodges, 2015). Quadtree grid nesting (Stelling, 2012; Volp et al., 2013) has been shown to reduce computational time, but application to flooding in complex urban terrains has not been tested. Sanders and Schubert (2019) proposed a full 2D dual (multi-grid) PRIMo model that employs bi-linear reconstruction of water-level within the coarse grid cells to improve the accuracy in flux estimation and to calculate the depth at fine-grid level (difference between the water-level and bed elevation). Here, the storage and friction versus water level look-up tables are populated for a few samples, including the deepest and highest fine-grid elevations. The fluxes are calculated for the subgrid cells along the edges of the coarse grid cell and are summed up. Sanders et al. (2022) and Schubert et al. (2022) have set up fine-resolution 3 m PRIMo models for Houston and Los Angeles at the metropolitan or mega-city scales, respectively. Information on the computational infrastructure was lacking in this paper. In Sanders and Schubert (2019), it can be seen that the supercomputing HPC cluster at the NCAR-Wyoming Supercomputing Center, which consisted of 36-core compute nodes with 2.3 GHz Intel Xeon processors and 64 GB of RAM, was used. Nevertheless, the study still underscores the need for a computationally efficient model in the case of using ensemble forecasts to reduce the input uncertainty. To quote the words of Schubert et al. (2022): "We note that modeling of ensembles is an example of embarrassingly parallel computations and can proceed quickly once a fast-running model is developed assuming adequate computational resources are available."

It has to be mentioned that the porosity approach not only defines the porosity values as the fraction occupied by the voids in the subgrid geometry (Sanders et al., 2008) but also fine-tunes them according to the numerical scheme used (Guinot, 2017b). On the other hand, the porosity-depth coupled approaches directly incorporate the subgrid volume and wetted face areas (Platzek et al., 2016), circumventing the need to calibrate or define the parametric porosity values. Thus, essentially, the porosity-based approach is different from the porosity-depth coupled approach. Nevertheless, the porosity-depth approach has been applied in various real-world cases (Li & Hodges, 2019; Platzek et al., 2016; Sehili et al., 2014). However, even in the recent developments of porosity approaches, large real-world urban areas with non-homogeneous layouts have not been tested and can be considered in the early stages of real-world application.

The city of Chennai belongs to a developing country (India) with unabated and uncontrolled urbanization. The city is highly populated, with several industries, hospitals, streets, highways, canals, major surface drains, etc. It experiences heavy, slow-rising floods in the monsoon months. Therefore, the pattern of urbanization is not spatially homogenous, making it challenging to implement an existing porosity-based approach directly to simulate flood inundation in the urbanized area, for a domain of considerable size (220 km^2). Similar conditions are also true for many other mega cities around the world. However, considering the availability of limited computing facilities, designing a reliable real-time flood forecasting system for such an urban area needs to be done. Outweighing the advantages and the practicality of the above-mentioned subgrid approaches, the model presented in the current study proposes a novel porosity-depth coupled approach but in a local-inertial SWEs framework (i.e., a subgrid-inertial model) (Bates et al., 2010; Sridharan et al., 2020), which does not exist till data. Such a subgrid-based local-inertial model (i.e., subgrid-inertial model) has the potential to be applied to highly urbanized areas like Chennai in the Global South. The computational advantage without sacrificing accuracy can be instrumental for urban flood forecasting to execute emergency action plans.

19447973, 2024, 5, Downloaded from https://agupubs.onlinelibrary.wiley.com/doi/10.1029/2023WR035334 by Helmholtz-Zentrum Potsdam GFZ, Wiley Online Library on [14/05/2024]. See the Terms and Conditions (https://onlinelibrary.wiley.com/terms-and-conditions) on Wiley Online Library for rules of use; OA articles are governed by the applicable Creative Commons License

In the subgrid-inertial model, the subgrid hydraulic variables are dynamically updated during the simulation based on the pre-stored relationships between the variables, such as volume, area, and the water surface elevation. The numerical scheme is modified to make it suitable for the local-inertial model. The novel algorithm is tested on idealized channels with various degrees of sinuosity and two real-world flood events. The subgrid definition of the within-grid complex urban terrain makes the proposed model more accurate and suitable for urban flood simulation than the existing coarse grid local-inertial models (i.e., course-inertial models) by resolving flooding around small-scale urban features like canals, streets, roads, highways, etc. Also, the proposed model simulations of inundation depths show accuracy close to full 2D models with several orders of computational advantage for floods in the subcritical flow regime. Notably, the proposed model is faster than existing local-inertial models of similar accuracy. In other words, the grid size of the existing local-inertial models must be finer to match the accuracy of the proposed subgrid-inertial model at a coarser grid size. It is noteworthy to mention that the proposed model differs from the existing subgrid and local-inertial models due to its implementation of the porosity-depth coupled approach in the light of local-inertial SWEs, construction of common interfaces, wet-dry check-in continuity and momentum equations, effective flow depth estimation, usage of polynomial fits to describe the subgrid bathymetry and assumption of a single free surface elevation within a coarse cell. Therefore, the proposed model has various features (elaborated in the upcoming sections) that are optimized to balance computational time and accuracy. Considering its accuracy and computational advantage, the proposed subgrid-inertial model is thus expected to be a new generation of urban flood simulation models.

2. Methodology

The lineage of local-inertial approximation of SWEs used in the proposed subgrid model traces back to Bates and De Roo (2000), that employed 1D kinematic wave approximation of the Saint-Venant equations for open channel flows and 2D continuity and Manning's equations for floodplain flows. Bates et al. (2010) refined it by solving the Saint-Venant equations but neglecting the convective acceleration for a computationally efficient simulation of slowly varying floods without compromising on accuracy. A semi-implicit mass flux estimation was introduced in order to avoid instabilities that may still occur in areas with shallow water depths, especially at the wet-dry interface (Bates et al., 2010; Kuiry et al., 2010). To further avoid numerical instabilities occurring in the simulations for low frictional regions (e.g., in urban environments), de Almeida et al. (2012) proposed an artificial diffusion by considering weighted mass fluxes between neighboring cells. The weightage parameter, θ, was considered to be a fixed value between 0.7 and 0.9, depending on the application problem. The local-inertial model developed following the above concepts is named LISFLOOD-FP and is freely downloadable (https://www.bristol.ac.uk/geography/research/hydrology/models/lisflood/). Later, Sridharan et al. (2020) derived an adaptive explicit expression θ that varies spatially and temporally depending on time step, local velocity and flow depth, and grid size, circumventing the need for calibration of θ for any applications. Sridharan et al. (2020) also observed that the adaptive weighting factor improves numerical stability and decreases overall computation time. The proposed model in this study employs a local-inertial approximation similar to Sridharan et al. (2020). In this study, a subgrid local-inertial model is developed for large-scale urban flood simulations with the aim of improved accuracy when compared to the traditional local-inertial models (Bates et al., 2010; Sridharan et al., 2020) and significant computational advantage with respect to full 2D models. The grid definitions, governing equations and their numerical solution, subgrid implementation, estimation of stable time step and advancement of solution with time are discussed in the following sections.

2.1. Coarse Grid and Subgrid Definitions

The mathematical model is developed by solving the local-inertial SWEs on a structured grid. A set of subgrid (i.e., the topographical grid) cells within a coarse grid (i.e., the numerical grid) cell constitute the computational domain. As the model runs on a structured coarse grid dependent on the available elevation raster data, the grid coarsening ratio r is the same in both x- and y-directions. Consider Δx and ΔX as the grid sizes of subgrid and coarse grid, respectively. The grid coarsening ratio r can be defined as $r = \Delta X/\Delta x$. The coarse and subgrid centroids are represented by the coordinates (I,J) and $(i,j)_k$, respectively. The value of k ranges from 1 to r^2. The bed elevation for the coarse cell and subgrid cells is defined as the average bed elevation of the subgrid cells.

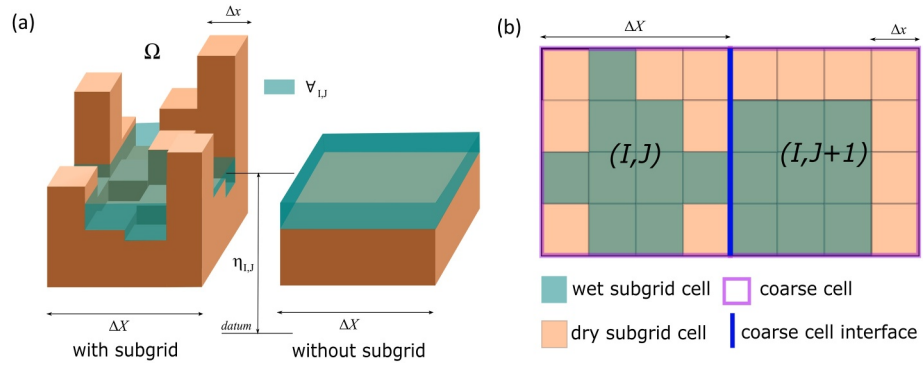

Figure 1. (a) Illustration of a coarse cell (I, J) with and without subgrid bathymetry, and (b) plan view of two neighboring coarse cells (I, J) and (I, $J+1$) with subgrid bathymetry.

2.2. Governing Equations

The proposed model solves the depth-averaged local-inertial 2D SWEs as given below (Bates et al., 2010; Sridharan et al., 2020).

$$\frac{\partial h}{\partial t}+\frac{\partial q_x}{\partial x}+\frac{\partial q_y}{\partial y}=0 \tag{1}$$

$$\frac{\partial q_x}{\partial t}+gh\frac{\partial \eta}{\partial x}+\frac{gn^2|q_x|q_x}{h^{7/3}}=0 \tag{2}$$

$$\frac{\partial q_y}{\partial t}+gh\frac{\partial \eta}{\partial y}+\frac{gn^2|q_y|q_y}{h^{7/3}}=0 \tag{3}$$

where h and η are the flow depth and free surface elevation from a datum, respectively; q_x and q_y are discharges per unit width along the x- and y-directions, respectively; g denotes the acceleration due to gravity, and n is Manning's friction coefficient.

The continuity Equation 1 can be expressed in vector form as

$$\frac{\partial h}{\partial t}+\nabla\cdot q=0 \tag{4}$$

where $q=\left(q_x,q_y\right)^T$ is the discharge per unit width in the normal direction to the common interface between two neighboring cells.

A set of subgrid cells (Figure 1a) within a coarse grid cell (Figure 1b) constitute the computational domain with the volume ∀ and flow depth h. Equation 4 is integrated over the coarse cell domain Ω (Figure 1), and on applying the Gauss divergence theorem to the second term, it reduces to,

$$\int_{\Omega}\frac{\partial h}{\partial t}d\Omega+\oint_{S}(q\cdot n)\,dS=0 \tag{5}$$

where S is the boundary of the domain Ω and n is the unit normal vector to S. As the domain (Figure 1) corresponds to a structured grid, Equation 5 can be discretized for the coarse cell (I, J) considering the cell volume ∀ as given below.

19447973, 2024, 5, Downloaded from https://agupubs.onlinelibrary.wiley.com/doi/10.1029/2023WR035334 by Helmholtz-Zentrum Potsdam GFZ, Wiley Online Library on [14/05/2024]. See the Terms and Conditions (https://onlinelibrary.wiley.com/terms-and-conditions) on Wiley Online Library for rules of use; OA articles are governed by the applicable Creative Commons License

$$\frac{\forall^{t+\Delta t}-\forall^{t}}{\Delta t}=\Delta X\left(\underbrace{q_{I-1/2,J}^{t+\Delta t}-q_{I+1/2,J}^{t+\Delta t}}_{\text{net flux in } x\text{-direction}}+\overbrace{q_{I,J-1/2}^{t+\Delta t}-q_{I,J+1/2}^{t+\Delta t}}^{\text{net flux in } y\text{-direction}}\right) \tag{6}$$

where the superscripts $t+\Delta t$ and t refer to the variables at current and previous time steps and Δt is the time step size. $q_{I-1/2,J}^{t+\Delta t}$ and $q_{I+1/2,J}^{t+\Delta t}$ represent the mass fluxes (q_x) along the x-direction through the interfaces ($I-1/2$,J) and ($I+1/2$,J), respectively. $q_{I,J-1/2}^{t+\Delta t}$ and $q_{I,J+1/2}^{t+\Delta t}$ denote the mass fluxes (q_y) along the y-direction through the interfaces (I,$J-1/2$) and (I,$J+1/2$), respectively.

The semi-implicit formulation proposed by de Almeida et al. (2012) and later modified by Sridharan et al. (2020) is utilized for computing mass fluxes q in Equation 6 through the interfaces of a coarse cell. For improved numerical stability and larger time step size, the upwind scheme that includes a fraction of the flux, denoted by θ, through the neighboring (in the upwind direction) cell interface is employed (de Almeida et al., 2012) for computing the mass flux. The mass flux at any interface, for example, through (I-1/2, J), is thus computed by solving the corresponding momentum equation (i.e., Equation 2 for x-direction and Equation 3 for y-direction) as

$$q_{I-1/2,J}^{t+\Delta t}=\begin{cases}\dfrac{\theta_{I-1/2}q_{I-1/2,J}^{t}+\left(1-\theta_{I-1/2}\right)q_{I-3/2,J}^{t}-gh_{\text{flow}}\Delta tS_{t}}{\left(1+gn^{2}\Delta t\left|q_{I-1/2,J}^{t}\right|/h_{\text{flow}}^{7/3}\right)}, \text{if } q_{I-1/2,J}^{t}>0\\ \dfrac{\theta_{I-1/2}q_{I-1/2,J}^{t}+\left(1-\theta_{I-1/2}\right)q_{I-1/2,J}^{t}-gh_{\text{flow}}\Delta tS_{t}}{\left(1+gn^{2}\Delta t\left|q_{I-1/2,J}^{t}\right|/h_{\text{flow}}^{7/3}\right)}, \text{if } q_{I-1/2,J}^{t}<0\end{cases} \tag{7}$$

where h_{flow} is the effective flow depth across the interface and S_t is the free surface gradient. It should be noted that Equation 7 at an interface is obtained from the discretized momentum equation (de Almeida et al., 2012; Sridharan et al., 2020) and considering its corresponding weighted value from the upwind interface. The expression for θ at an interface is derived by Sridharan et al. (2020) as

$$\theta_{I-1/2,J}=1-\frac{\Delta t}{\Delta X}\min\left(\frac{\left|q_{I-1/2,J}\right|}{h_{\text{flow}}},\sqrt{gh_{\text{flow}}}\right) \tag{8}$$

The effective flow depth, h_{flow}, is estimated at the interfaces of a coarse cell based on the available wetted face area per unit width (i.e., interface length) as,

$$h_{flow}=\frac{\text{wetted face area at }\eta_{\max}}{\Delta X} \tag{9}$$

where $\eta_{\max}$ represents the maximum of the water surface elevations of the coarse cells on either side of an interface. The computation of h_{flow} herein is entirely different from Sridharan et al. (2020) in order to account for the variation in subgrid bed elevation along an interface. First, the maximum of the free surface elevations in the coarse cells for the previous time step on either side of the interface is obtained. Then, it is substituted into the pre-stored face area versus free surface elevation relationship of the considered interface to arrive at the wetted face area. The wetted face area per unit width (i.e., interface length) then gives the h_{flow} at the interface. There can be different alternatives to estimate h_{flow}, but the above definition is found to compute the right amount of mass flux during the computation, and it does not result in any numerical instability.

2.3. Pre-Stored Face Area, Volume, and Water Surface Elevation Relationships

Before execution of the model setup with a new coarse grid size and/or a new domain, a preprocessing algorithm is run to process the within-grid information using polynomial fits and store the polynomial coefficients for each coarse cell. In the momentum equation, it is required to know the face area based on the water surface elevation. In the continuity equation, based on the wetted volume, the water surface elevation within the cell needs to be estimated. Therefore, in the preprocessing algorithm, a moving window with the size of the coarse grid is allowed

19447973, 2024, 5, Downloaded from https://agupubs.onlinelibrary.wiley.com/doi/10.1029/2023WR035334 by Helmholtz-Zentrum Potsdam GFZ, Wiley Online Library on [14/05/2024]. See the Terms and Conditions (https://onlinelibrary.wiley.com/terms-and-conditions) on Wiley Online Library for rules of use; OA articles are governed by the applicable Creative Commons License

19447973, 2024, 5, Downloaded from https://agupubs.onlinelibrary.wiley.com/doi/10.1029/2023WR035334 by Helmholtz-Zentrum Potsdam GFZ, Wiley Online Library on [14/05/2024]. See the Terms and Conditions (https://onlinelibrary.wiley.com/terms-and-conditions) on Wiley Online Library for rules of use; OA articles are governed by the applicable Creative Commons License

to slide over the high-resolution data and for each elevation in the subgrid cells, the volume and the face area are calculated as described in the following text.

The volume of water, $\forall_{I,J}$, corresponding to each coarse cell for known $\eta_{I,J}$ is defined as,

$$\forall_{I,J} = \sum_{k=1}^{r^2} \max\left(\eta_{I,J} - z_{i_j{}_k}, 0\right) \times \Delta x \times \Delta x \tag{10}$$

where $z_{i_j{}_k}$ represents the average bed elevation of kth subgrid cell contained within the coarse cell (I, J).

In the case of a raster-based grid, the cell interfaces will have different sets of average bed elevation on their left and right sides due to the subgrid definition of topography along the interface (Figure 1). The common wetted face area for the water surface elevation η is then estimated as,

$$Wetted\ face\ area = \sum_{k=1}^{r} \max(\eta - z_{\max_k}, 0) \times \Delta x \tag{11}$$

where $z_{\max_k}$ represents the maximum of the bed elevations of two kth neighboring subgrid cells on either side of the coarse cell interface and η represents the free surface elevation for which the wetted face area is calculated.

The volume and face areas for different subgrid elevations are thus calculated and tabulated for each coarse cell. After several trials with various non-linear fits between subgrid variables and elevation, it was found that polynomial fits are accurate. Second and third-degree polynomial fits for elevation (as x) versus face area (as y) and volume (as x) versus elevation (as y) are obtained, respectively. The polynomial coefficients are thus estimated and prestored for each coarse cell and are then used during the execution of the program. It has to be noted that the determination of the relationships between free surface elevation and subgrid geometry variables (i.e., $\forall_{I,J}$ and h_{flow}) for each coarse cell and storing them before execution of the algorithm saves computation cost (Li & Hodges, 2019; G. Wu et al., 2016).

During the simulation, the free surface elevation at any time within the coarse cell is assumed to be constant (Casulli, 2009). Therefore, as a post-processing reprojection step, the flow depths in the subgrid cells are calculated for the inundation extent as follows,

$$h_{i_j{}_k} = \max\left(\eta_{I,J} - z_{i_j{}_k}, 0\right), \text{ for } k = 1,2,..., r^2 \tag{12}$$

where r represents the grid coarsening ratio and r^2 is the total number of sub-grid cells within a coarse grid cell. Thus, the subgrid cells with bed elevation greater than their corresponding coarse grid cells' free surface elevation are considered dry.

2.4. Time Step Estimation

The proposed numerical method is explicit in nature, and hence, the time step is calculated according to the following adaptive expression,

$$\Delta t = \alpha \frac{\Delta X^2}{\sqrt{g \forall_{\max}}} \tag{13}$$

where $\forall_{\max}$ is the maximum estimated volume in the previous time step in the entire domain and α is the CFL number. Equation 13 uses volume instead of depth in the time step formulation, as suggested by Bates et al. (2010). According to Bates et al. (2010) and de Almeida et al. (2012), this is a necessary but not sufficient condition for stability. It needs to be mentioned that an improved stability condition may be derived for the subgrid-inertial model.

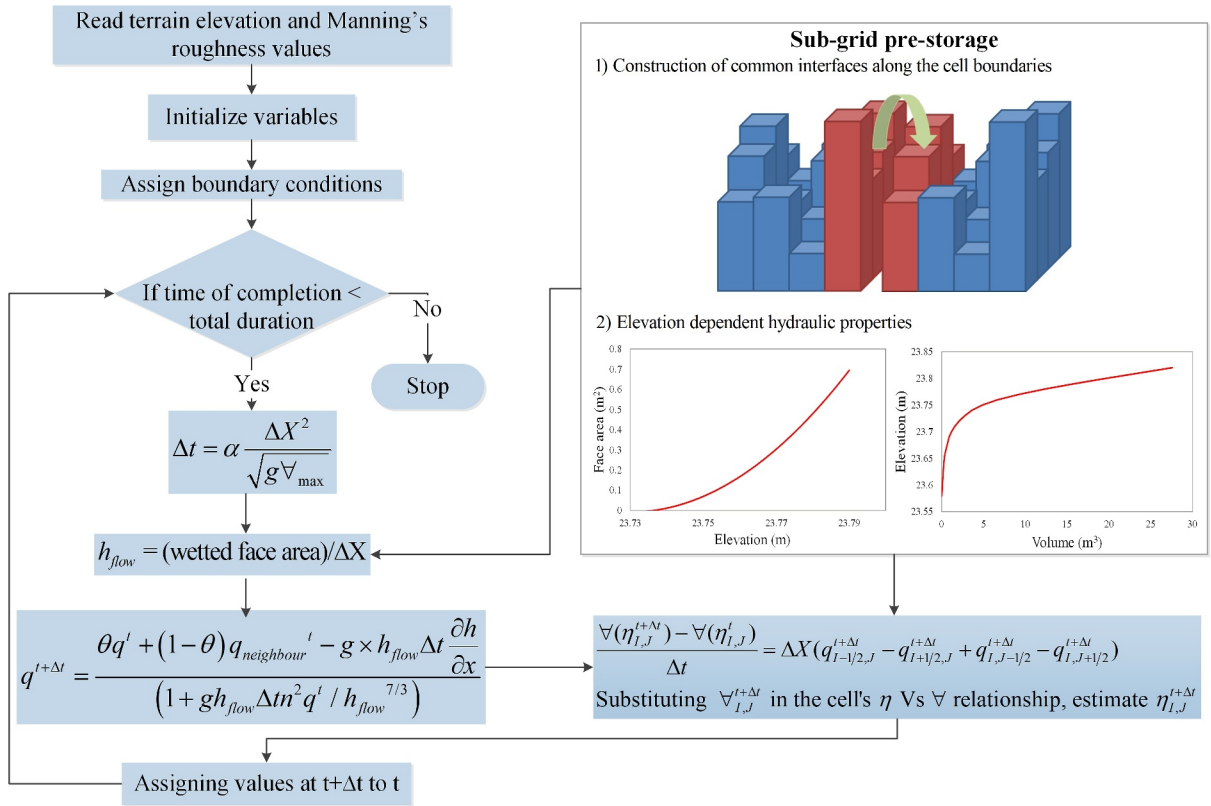

Figure 2. Steps involved in the proposed subgrid algorithm.

2.5. Implementation of the Subgrid Algorithm

The proposed subgrid local-inertial model actually solves the simplified SWEs (Equations 1–3) on a coarser grid. The preprocessing algorithm mentioned in the previous section is run before the execution of the model only when a new grid size and/or a new domain is chosen. The following are the steps that are described in the order of execution during the simulation,

1. Based on the supplied initial conditions, the hydraulic variables of the coarse cells are initialized only once at the beginning of the model execution. Then, at the beginning of every time step, the boundary conditions are assigned.
2. The time step is calculated using Equation 13. After that, the model moves to the computation of mass fluxes through the cell interfaces at the current time step. In this step, first, the maximum of the free surface elevations of the previous time step on either side of a cell interface is computed. Then, this value is substituted in the pre-stored face area versus water surface elevation polynomial fit to compute effective flow depth for that interface using Equation 9. The effective flow depth is then used to compute mass fluxes through the interface using Equation 7. The same computations are repeated for all the cell interfaces.
3. Lastly, Equation 6 is solved for the wetted volume at the current time step by updating the volume at the previous time step based on the current time step mass fluxes through the interfaces of the coarse cell. By substituting the updated volume at the current time step in the pre-stored volume versus water surface elevation polynomial fit, the free surface elevations for the coarse cells at the current time step are obtained.

Thus, the solution is advanced with time for unknown free surface elevation, and these steps are executed in a loop till the specified event duration is reached. Figure 2 summarizes the overall framework of the proposed subgrid solution algorithm. Further, when the $\forall_{I,J}^{t+\Delta t}$ is greater than the maximum volume that can be contained within the subgrid bathymetry, then a cube geometry is considered beyond the subgrid bathymetry to estimate $\eta_{I,J}^{t+\Delta t}$. From Figures 1 and 2, it can be clearly seen that the proposed subgrid algorithm effectively incorporates the high-resolution bathymetry within the coarse grid with the aid of pre-stored elevation-dependent hydraulic

19447973, 2024, 5, Downloaded from https://agupubs.onlinelibrary.wiley.com/doi/10.1029/2023WR035334 by Helmholtz-Zentrum Potsdam GFZ, Wiley Online Library on [14/05/2024]. See the Terms and Conditions (https://onlinelibrary.wiley.com/terms-and-conditions) on Wiley Online Library for rules of use; OA articles are governed by the applicable Creative Commons License

properties. Thus, the coarse grid without subgrid implementation fails to do so as it uses one single averaged bed elevation for each coarse cell. Due to the implementation of the subgrid concept, the mass flux computation through an interface is more accurate than a coarse-inertial model. As a result, better accuracy of the proposed subgrid-inertial model becomes obvious.

The flood wave propagation is a process of wetting-drying at the waterfront. Therefore, the following robust wetting-drying algorithm has been implemented:

- The mass flux at an interface for the current time step $q^{t+\Delta t}$ is set to zero, and its estimation is skipped when both the free surface elevations of the cells on either side of the interface are less than the minimum most bed elevation of the common interface.
- In the estimation of water surface elevation $\eta_{I,J}$, a coarse cell is considered wet when its $\eta_{I,J}$ exceeds the minimum bed elevation of all the contained subgrid cells within the extent of the coarse cell. This helps in the correct assessment of the coarse cell's dry/wet status (Li & Hodges, 2019).

Thus, these checks exclude dry, coarse cells by considering all the subgrid cells that lie within them from becoming a part of the solution. Also, these checks prevent unphysical flows through an interface and allow for realistic estimation of the mass flux.

The salient features of the proposed subgrid-inertial model are summarized as follows:

1. The porosity-depth coupled approach of Casulli (2009) is used in this local-inertial approximation of SWEs. The relationship of the subgrid variables (volume and face area in x- and y-directions) with respect to free surface elevations are represented using polynomial fits. After several trials with various non-linear fits, the polynomial fits best represented the relationships. The polynomial coefficients defining the subgrid relationships are precalculated for each cell and its faces and pre-stored. G. Wu et al. (2016) used a similar pre-storage method for porosity versus free surface relationships to reduce the simulation time significantly. In contrast, in the proposed model, the relationships between the hydraulic variables (volume and face area) and the free surface relationships are pre-stored. These pre-stored values are later used during the execution of the proposed model, thus facilitating a direct representation of the subgrid bathymetry. Such a simultaneous updating of subgrid variables with free surface elevation ensures mass conservation (Casulli, 2009).
2. In the study conducted by Li and Hodges (2019), which utilized a porosity-depth coupled approach on a structured grid for the continuous modeling of salinity transport, blockages along the interface were considered by assigning zero to the subgrid face area. However, the computed wetted face area still depended on the side of the interface for which the mass flux calculation was performed. In the proposed model, a common edge that is the maximum of the bed elevations of the subgrid cells on either side of the interface is constructed. The wetted face area of this common edge for different free surface elevations is used in the earlier preprocessing steps. Further, for an accurate representation of wetting and drying, the fluxes are set to zero when both the free surface elevations of the cells on either side of the interface are less than the minimum most bed elevation of the common edge. This not only accounts for the flow blockage along the interface but also aids in a realistic mass flux computation.
3. The proposed effective flow depth (h_{flow}) formulation that is calculated based on the wetted face area along the constructed common interface mainly contributes to improving the accuracy of flood inundation simulation compared to the existing coarse-inertial model that naively averages out within grid terrain elevations (please refer to Supporting Information S1).
4. The proposed model operates entirely in terms of free surface elevation, and a single horizontal free surface elevation for a coarse cell is used in every time step. To elaborate, the free surface elevation from the previous time step is used in the momentum equation for flux estimation. Herein, the pre-stored face area versus free surface elevation of the common edge is used. The estimated fluxes at the current time step are used in the continuity equation to estimate volume. The volume at the current time step is eventually used in the calculation of free surface elevation at the current time step using the prestored free surface elevation versus volume relationship, and so on and so forth.

Thus, the proposed model differs from the existing models due to its implementation of the porosity-depth coupled approach in local-inertial SWEs, construction of common interfaces, wet-dry check-in continuity and momentum equations, usage of polynomial fits to describe the subgrid bathymetry and assumption of a single free surface elevation within a coarse cell. It has to be noted that according to Sanders and Schubert (2019), a

19447973, 2024, 5, Downloaded from https://agupubs.onlinelibrary.wiley.com/doi/10.1029/2023WR035334 by Helmholtz-Zentrum Potsdam GFZ, Wiley Online Library on [14/05/2024]. See the Terms and Conditions (https://onlinelibrary.wiley.com/terms-and-conditions) on Wiley Online Library for rules of use; OA articles are governed by the applicable Creative Commons License

19447973, 2024, 5, Downloaded from https://agupubs.onlinelibrary.wiley.com/doi/10.1029/2023WR035334 by Helmholtz-Zentrum Potsdam GFZ, Wiley Online Library on [14/05/2024]. See the Terms and Conditions (https://onlinelibrary.wiley.com/terms-and-conditions) on Wiley Online Library for rules of use; OA articles are governed by the applicable Creative Commons License

horizontal water level throughout the coarse grid is a good approximation for most floods. The reprojection of depth for subgrid cells at every time step can be done only when the fine-resolution inundation depths are needed at a time step, as the equations are solved in terms of elevation. Nevertheless, at the end of the simulation, a reprojection step considering a horizontal water surface elevation within the coarse cell is adopted to arrive at an accurate maximum inundation depth for the subgrid cells. This post-processing step is important for an accurate assessment of the flood inundation extent and hazard. As a future scope, a block-checking procedure similar to Li and Hodges (2019) can be implemented to improve the accuracy of the model further.

Essentially, the proposed subgrid-inertial model can represent the high-resolution topography that cannot be represented by using a coarser numerical grid alone, thereby increasing the accuracy of the simulated inundation extent. Thus, in the context of urban floodplains, the subgrid-inertial model can help capture flooding along complex terrain features of the urban infrastructure. This information is missed by the coarse-inertial models that naively average the within-grid terrain data.

3. Results and Discussion

The developed subgrid-inertial model is extensively evaluated for its accuracy and applicability to flood inundation problems with a focus on urban floods. The model results are compared with the observed data. Nevertheless, in certain urban flooding scenarios, observed data are limited, and in such a situation, the intercomparison of different model outputs is investigated. For this purpose, three model setups, as discussed below, are considered:

1. *Subgrid-inertial model setup*—the model setup refers to the developed local-inertial model using the subgrid approach. The model setup is run on different grid resolutions for the test cases described below. The "*subgrid* ×*m*" denotes the subgrid local-inertial model simulation, where × represents the numerical grid size in meters.
2. *Coarse-inertial model setup*—the model setup refers to the local-inertial model developed by Sridharan et al. (2020), which is very similar to the LISFLOOD-FP (Bates et al., 2010; De Almeida et al., 2012) except for the implementation of an analytical expression for the weighting factor. This expression makes the model of Sridharan et al. (2020) computationally more efficient. The LISFLOOD-FP was upgraded by Rong et al. (2022) following the development suggested by Sridharan et al. (2020). It has to be highlighted that the coarse-inertial model setup naively averages out the topography within the grid without accounting for subgrid terrain variations. The "*coarse* ×*m*" denotes the existing local-inertial model (Sridharan et al., 2020) simulation, where × represents the numerical grid size in meters.
3. *HEC-RAS model setup*—the model setup refers to the freely downloadable HEC-RAS 2D model (USACE, 2016). The "*HEC-RAS* ×*m*" denotes the HEC-RAS full 2D model simulation that uses high-resolution elevation data at fine grid sizes, where × represents the grid size in meters. Also, HEC-RAS simulations are considered benchmark solutions in cases where observed data are not available.

The subgrid-inertial model is tested for various test cases, as described below.

1. *Flow in idealized sinuous channels*—Canestrelli et al. (2012) showed that simplified numerical schemes can't capture the backwater profile in a meandering or sinuous river, and they tend to overpredict the water levels upstream. The error increases as the sinuosity (defined as the ratio between channel length and down valley length of the river) increases. In this test, the proposed model is then analyzed for simulating water levels along the river for a range of sinuosity 1–8.5. The results for this analytical test case are presented in Supporting Information S1.
2. *Urban flooding in Carlisle city, UK*—flooding in the interconnected rivers Eden, Caldew, and Petteril flowing through moderately urbanized Carlisle city (14.5 km^2) in the UK is considered. The real flood event in the urbanized setting is simulated to investigate the accuracy of the proposed model in predicting water levels and maximum flood extent and computational cost compared to the high-resolution full 2D simulation by HEC-RAS and coarse-inertial model.
3. *Urban flooding of Adyar River in Chennai city, India*—flooding in the Adyar River, connected with major and minor canals flowing through the highly urbanized Chennai city (220 km^2) in the state of Tamil Nadu, India, is considered. The large-scale flood study was conducted in a fully urbanized city to ensure the applicability of the model after validation with the limited observed data. The computational efficiency of the model is investigated with respect to the high-resolution full 2D simulation by HEC-RAS and the coarse-inertial model.

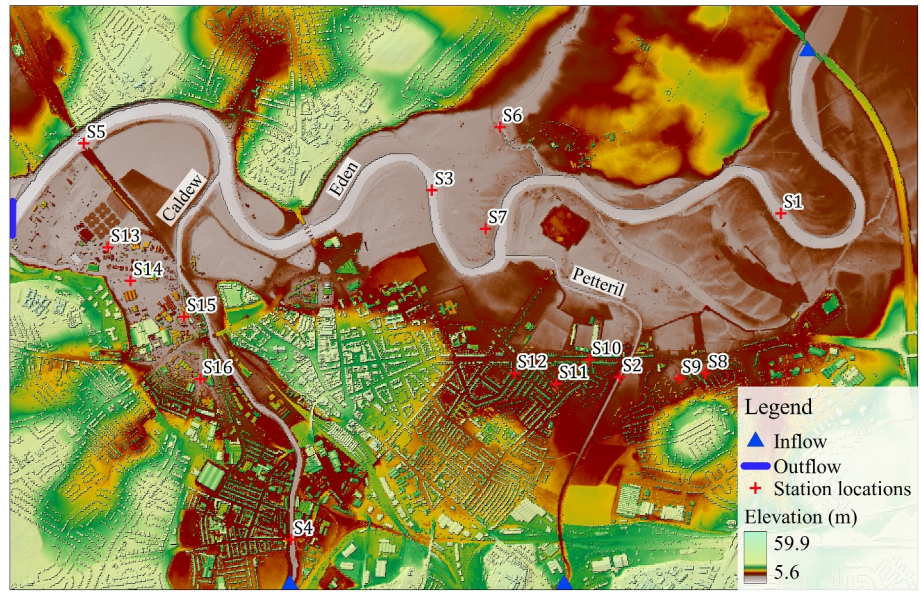

Figure 3. Map showing Carlisle city's 5 m elevation data set, inflow and station locations, and gauge locations (S1 to S16).

4. *Explanation for the improvement in accuracy*—An investigation has been undertaken to determine the factors contributing to the improved accuracy of the proposed subgrid-inertial model in urban flood simulations compared to the coarse-inertial model. The examination focuses on determining whether the improved accuracy can be attributed to the inclusion of reprojection step, subgrid-wetted volume, or subgrid-wetted face area. The analysis specifically considers the flooding in Chennai city, as described in Section 3.2, for this purpose. The detailed findings of this investigation are presented in Supporting Information S1.

All the simulations were performed on a desktop with 16 GB RAM and a 3 GHz AMD Ryzen 9 4900HS processor.

3.1. Urban Flooding in Carlisle City, UK

The proposed subgrid model is applied to simulate an important 36-hr duration flooding event in the city of Carlisle, UK (Figure 3). The major inflows into the city are from the river Eden, which flows from east to west across the hydraulic domain that comprises the city. Two more rivers, namely, Caldew (leftmost) and Petteril (rightmost), enter the domain from the southern boundary, further bringing inflows into the city (Figure 3). Heavy rainfall on 6–7 January 2005 over the catchment of the river Eden affected nearly 3,500 homes altogether (Neal, Bates, et al., 2009; Neal, Fewtrell, & Trigg, 2009). Mason et al. (2007) have generated a digital elevation data set inclusive of the buildings at a spatial resolution of 5 m, using LiDAR. The surveyed river cross-sections were subsequently burned into the data set (Mason et al., 2007). The chosen grid sizes for the analysis are 5, 10, 20, 30, 40, 50, 60, 70, 80, and 90 m for the coarse-inertial model. However, the subgrid-inertial model is run only on 30, 60, and 90 m grids with the r values of 6, 12, and 18, considering its accuracy. Manning's n values of 0.055 $m^{-1/3}s$ and 0.06 $m^{-1/3}s$ are used for the rivers and floodplains as adapted in Neal, Fewtrell, and Trigg (2009) and Neal, Bates, et al. (2009). To comprehensively assess the accuracy of the proposed model, the HEC-RAS full 2D model with a 5 m semi-structured grid is first calibrated and validated for the flooding event and used as the reference solution. For this purpose, the observed maximum and time-series of water level data at different gauge stations are used. The stations are in the rivers (S1 to S5) and on the floodplains (S7 to S16), as shown in Figure 3. The stations S6 and S7 are located on the floodplains of the river Eden, devoid of urban features. The stations located on the urbanized floodplains of the rivers Petteril and Caldew are S8 to S12 and S13 to S16, respectively. In addition to the gauge data, flood marks were collected soon after the flooding event. Some flood marks were collected close to the gauges, and some were collected within a 100 m distance. The simulated results of the subgrid-inertial model are compared with those from the reference fine-grid HEC-RAS and coarse-inertial models and observed data. This is done to understand the ability of the subgrid-inertial algorithm to capture the flow dynamics influenced by the smaller urban terrain features at different grid resolutions.

19447973, 2024, 5, Downloaded from https://agupubs.onlinelibrary.wiley.com/doi/10.1029/2023WR035334 by Helmholtz-Zentrum Potsdam GFZ, Wiley Online Library on [14/05/2024]. See the Terms and Conditions (https://onlinelibrary.wiley.com/terms-and-conditions) on Wiley Online Library for rules of use; OA articles are governed by the applicable Creative Commons License

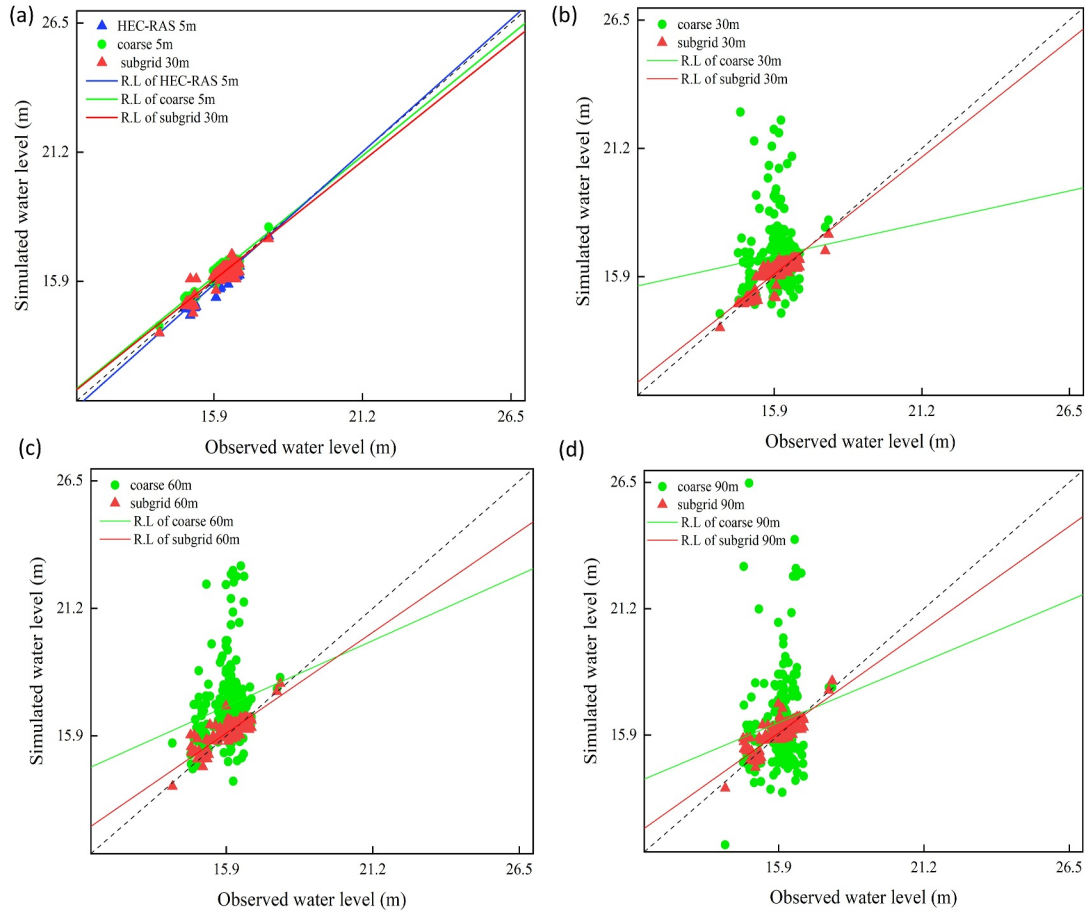

Figure 4. Scatter plots of observed and simulated maximum water levels for different models: (a) model setups of similar accuracy; coarse and subgrid-inertial model setups at (b) 30 m, (c) 60 m, and (d) 90 m. R.L represents the regression line between the simulated and observed scatter.

3.1.1. Comparison of Floodwater Marks and Time-Series of Water Levels

Comprehensive surveys using the differential Global Positioning System were conducted post-flooding for floodwater marks. The water levels at the three gauges (S2, S4 and S5) located in the rivers, as shown in Figure 3, were recorded during the event. The data sets are reported in Neal, Fewtrell, and Trigg (2009) and Neal, Bates, et al. (2009). It should be noted from the spread around the 1:1 in the observed flood marks and simulated maximum water level scatter plots in Figure 4 at selected resolutions that the proposed subgrid-inertial model is seen to perform significantly better than the coarse-inertial model. The observed and simulated maximum water levels (i.e., flood marks) are compared for all the models, and the R^2 and RMSE values are summarized in Tables 1 and 2. As expected, the reference *HEC-RAS* 5m model setup reported the highest accuracy against the measured data, with R^2 and RMSE values of 0.82 and 0.24 m, respectively. The proposed subgrid-inertial model is found to consistently produce higher accuracy compared to the coarse-inertial model of similar grid size. The accuracy of coarse-inertial and subgrid-inertial models are comparable to that of HEC-RAS reference and observed data at 5 and 30 m resolutions, respectively (Figure 4a). However, the accuracy of the coarse-inertial model degrades as the resolution become coarser than 10 m (Figures 4b–4d). In other words, the *coarse* 5m, *subgrid* 30m, and *HEC-RAS* 5m model setups perform similarly for the simulation of maximum water levels.

To further assess the accuracy of the developed model, the time-series of water levels obtained by the subgrid-inertial model are plotted in Figure 5 along with that from the reference HEC-RAS and coarse-inertial simulated results, and recorded time-series of water levels at some gauges. For better clarity, the comparison is shown only at selected resolutions, as shown in Figure 5. The subgrid-inertial model can even capture the trend of water level variations at the resolutions 30 m, 60 and 90 m, whereas the coarse-inertial model setup fails at most of the

19447973, 2024, 5, Downloaded from https://agupubs.onlinelibrary.wiley.com/doi/10.1029/2023WR035334 by Helmholtz-Zentrum Potsdam GFZ, Wiley Online Library on [14/05/2024]. See the Terms and Conditions (https://onlinelibrary.wiley.com/terms-and-conditions) on Wiley Online Library for rules of use; OA articles are governed by the applicable Creative Commons License

19447973, 2024, 5, Downloaded from https://agupubs.onlinelibrary.wiley.com/doi/10.1029/2023WR035334 by Helmholtz-Zentrum Potsdam GFZ, Wiley Online Library on [14/05/2024]. See the Terms and Conditions (https://onlinelibrary.wiley.com/terms-and-conditions) on Wiley Online Library for rules of use; OA articles are governed by the applicable Creative Commons License

Table 1
Performance Metrics for Coarse Models of Different Grid Sizes up to 90 m

Model	R^2	RMSE (m)	MAR_Pdiff (%)	MAR_Tp (%)	F (%)	Time taken (s)	Relative time
HEC-RAS 5m	0.88	0.24	Ref.	Ref.	Ref.	149,579	361.3
coarse 5m	0.88	0.26	0.85	2.22	95	8,697	21.01
coarse 10m	0.38	0.98	3.09	2.26	86	1,290	3.12
coarse 20m	0.12	1.22	4.69	11.1	85	248	0.6
coarse 30m	0.09	1.65	6.33	16.33	81	120	0.29
coarse 40m	0.06	1.79	6.59	22.1	80	89	0.21
coarse 50m	0.04	1.83	7.19	28.15	80	67	0.16
coarse 60m	0.03	1.95	7.75	28.4	78	50	0.12
coarse 70m	0.02	2.07	8.22	22.17	77	45	0.11
coarse 80m	0.02	2.23	8.34	22.11	76	37	0.09
coarse 90m	0.02	2.59	8	38.77	72	28	0.07

gauges for these large grid sizes (Figure 5). On the other hand, only a fine resolution grid size coarse model, namely, the *coarse* 5m model setup simulates water-levels closer to that of the *HEC-RAS* 5m model setup. Thus, the advantages of applying a subgrid-inertial model at larger grid sizes can be easily realized.

In stations in the rivers Eden (S5), Caldew (S4) and Petteril (S2), the accuracy of the coarse-inertial model is poor, whereas the subgrid-inertial model setup is closer to the reference. The coarse-inertial and subgrid-inertial model setups' results are closer to the reference only at the two stations in the main River Eden (S1 and S3). At stations S6 and S7 on the non-urbanized flood plain of the river Petteril, the simulated water levels by the coarse-inertial model are again poor, and the subgrid-inertial model better captures the trend of water-level variations. The stations S8 to S12 are located on the urbanized flood plains of river Petteril. For stations S8 to S10, only the *coarse* 30m simulated water levels and *coarse* 60 and 90m reported no flooding. Even then, at stations S8 and S10, the pattern of *coarse* 30m simulated water levels did not match that of the HEC-RAS and observed data. In addition, the coarse-inertial model does not simulate any inundation at stations S11 and S12. Similarly, the simulated water levels by the coarse-inertial model are away from the HEC-RAS results and observed data in the remaining stations S13-S16, located on the urban flood plains of the river Caldew. The poor accuracy of the coarse-inertial model may be attributed to the fact that when the within-grid terrain elevations are aggregated, the topographical features are not represented accurately. As a result, the hydraulic connectivity between the grid interfaces is lost or misrepresented. Eventually, this gets reflected in the flow dynamics while computing the mass fluxes. In Figure 5, we can see that the gauge elevations are completely different for some grids. It has to be noted that the time-series are presented as water levels rather than as depths to facilitate comparison with observed stage values. Therefore, the water levels show different initial values for model setups of different grid sizes due to grid coarsening. On the other hand, the differences with respect to fine grid reference are lesser for the subgrid-inertial model that assumes the initial level to be that of the minimum most cell elevation within the coarse grid. Thus, the developed subgrid-inertial model with large grid sizes (30, 60, and 90 m) not only maintains better accuracy than the coarse-inertial model of similar grid size in all the stations but also captures the flood inundation of the urbanized flood plains. To reiterate, the subgrid-inertial model at large grid sizes can simulate water levels close to the available observed water level recordings, *HEC-RAS* 5m and *coarse* 5m results at all the stations located in Petteril, Caldew, and Eden Rivers and their flood plains. The subgrid-inertial model allows for the utility of a larger grid size than the coarse-inertial model to achieve reasonable accuracy in flood simulation in urbanized flood plains.

Table 2
Performance Metrics for Subgrid Models of Different Grid Sizes

Model	R^2	RMSE (m)	MAR_Pdiff (%)	MAR_Tp (%)	F (%)	Time taken (s)	Relative time
subgrid 30m	0.81	0.27	0.85	2.83	94	414	1
subgrid 60m	0.75	0.29	0.86	3	92	171	0.41
subgrid 90m	0.73	0.31	0.88	3.02	89	94	0.23

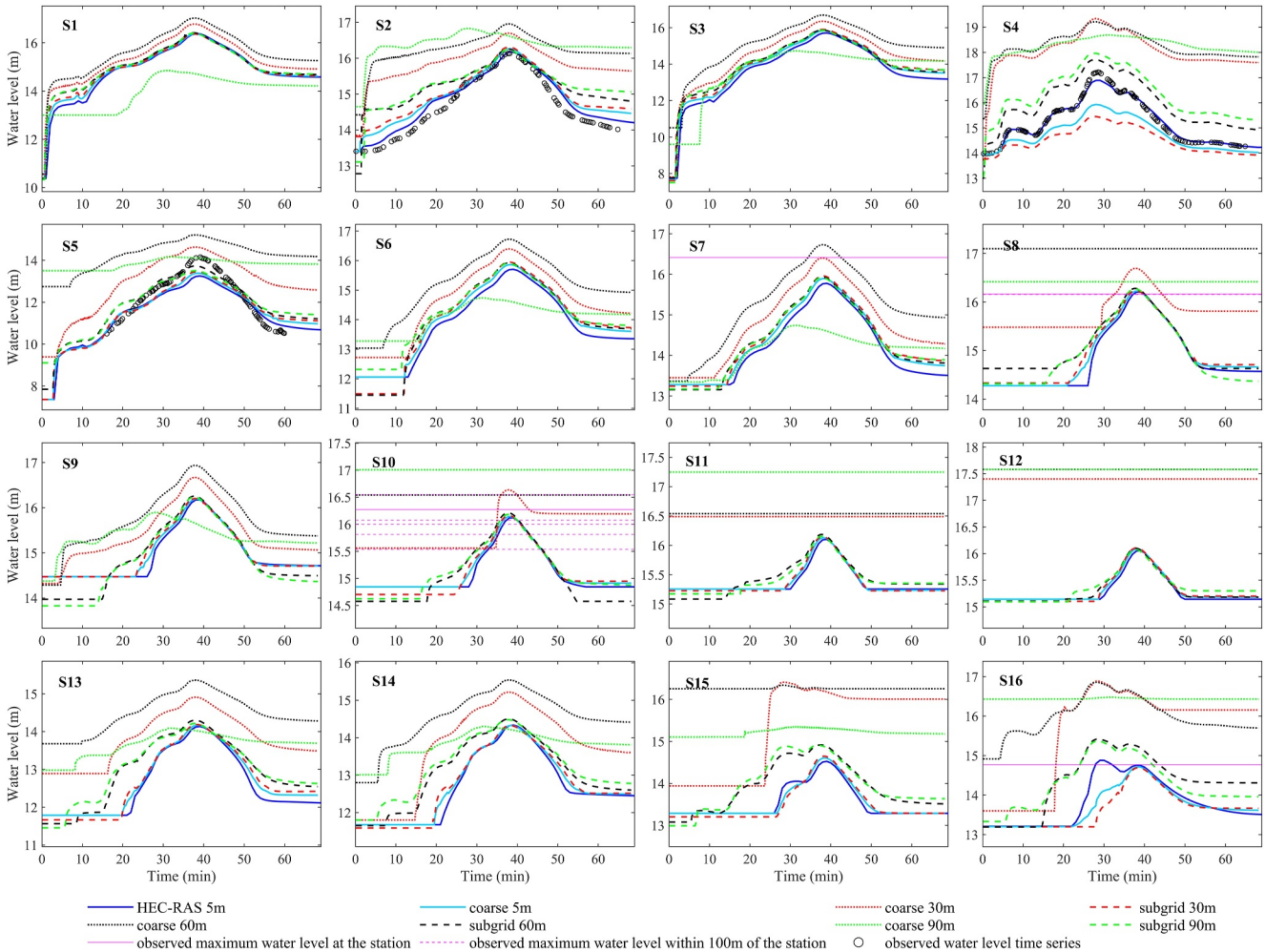

Figure 5. Water level time series of various models at the 16 stations. The observed time series or maximum water level at the station or maximum water levels within 100 m of the station are plotted based on availability.

Further, the time to peak and the difference in the peak value with respect to the HEC-RAS reference solution are denoted as MAR_Tp and MAR_Pdiff. The indices, MAR_Tp and MAR_Pdiff are estimated as follows,

$$\text{MAR\_Tp}(\%) = \sum_{n} \frac{\left|(Tp_o - Tp_s)/Tp_o\right|}{n} \times 100 \tag{14}$$

$$\text{MAR\_Pdiff}(\%) = \sum_{n} \frac{\left|(P_o - P_s)/P_o\right|}{n} \times 100 \tag{15}$$

where Tp_o and Tp_s represent the time to peak of HEC-RAS full2D and local-inertial models at each station, respectively; n represents the total number of stations considered for analysis; P_o and P_s represent the peak inundation depth of HEC-RAS full2D and local-inertial models at each station, respectively. These values are compared to investigate the accuracy of the local-inertial models in Tables 1 and 2. It has to be noted that the R^2 and RMSE indices are calculated with respect to observed water levels, while the MAR_Tp and MAR_Pdiff are with respect to the reference HEC-RAS full 2D simulation. It is also evident from Tables 1 and 2 that the *subgrid* 30m setup can produce results with similar accuracy of *coarse* 5m and *HEC-RAS* 5m setups.

19447973, 2024, 5, Downloaded from https://agupubs.onlinelibrary.wiley.com/doi/10.1029/2023WR035334 by Helmholtz-Zentrum Potsdam GFZ, Wiley Online Library on [14/05/2024]. See the Terms and Conditions (https://onlinelibrary.wiley.com/terms-and-conditions) on Wiley Online Library for rules of use; OA articles are governed by the applicable Creative Commons License

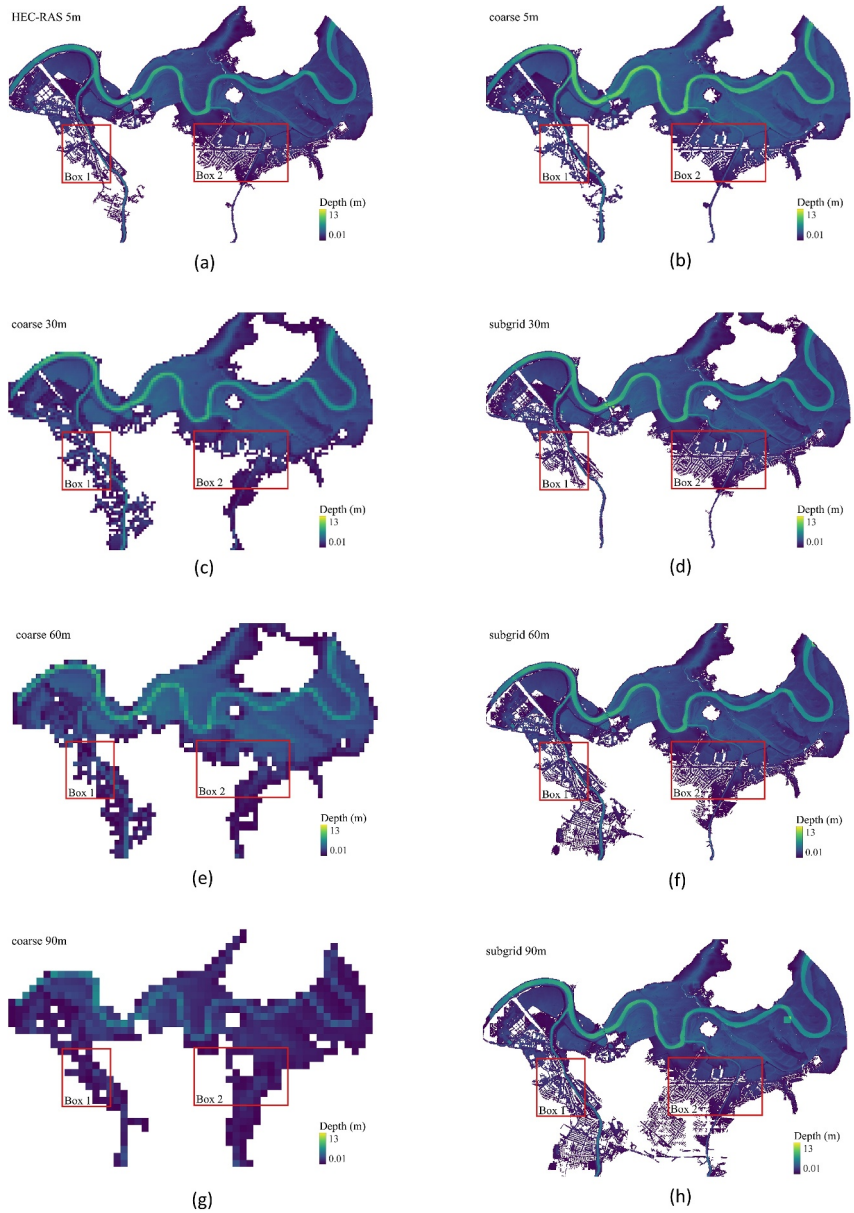

Figure 6. Maximum inundation extents simulated by the (a) HEC-RAS 5m, (b) coarse 5m, (c) coarse 30m, (d) subgrid 30m, (e) coarse 60m, (f) subgrid 30m, (g) coarse 90m, and (h) subgrid 90m. Boxes 1 and 2 show the urban areas, consisting of buildings and streets, situated on the flood plains of the rivers Caldew and Petteril, respectively.

3.1.2. Comparison of the Maximum Inundation Extent

As the maximum inundation map of the event is not available, the inundation map of the HEC-RAS simulation on 5 m DEM is considered the reference solution for model comparisons. Figure 6 shows the maximum inundation depth maps of all the models at different resolutions. The areas within boxes 1 and 2 correspond to urban areas consisting of buildings, streets, roads, etc., in the vicinity of the rivers Caldew and Petteril. The large grid subgrid-inertial model can simulate flooding, resolving finer urban features in these areas. In contrast, the coarse-inertial model of similar grid size misses out on the small terrain features. Visually, it can be seen that the inundation extents from *coarse* 5m and *subgrid* 30m match well with that of the reference *HEC-RAS* 5m. The agreement of the simulated maximum inundation extents with that of the reference solution is presented in Figure 7 by highlighting the underprediction, overprediction and match between them. With the increase in grid size, the subgrid-inertial model shows less under and more overprediction. The overprediction by the subgrid-inertial

19447973, 2024, 5, Downloaded from https://agupubs.onlinelibrary.wiley.com/doi/10.1029/2023WR035334 by Helmholtz-Zentrum Potsdam GFZ, Wiley Online Library on [14/05/2024]. See the Terms and Conditions (https://onlinelibrary.wiley.com/terms-and-conditions) on Wiley Online Library for rules of use; OA articles are governed by the applicable Creative Commons License

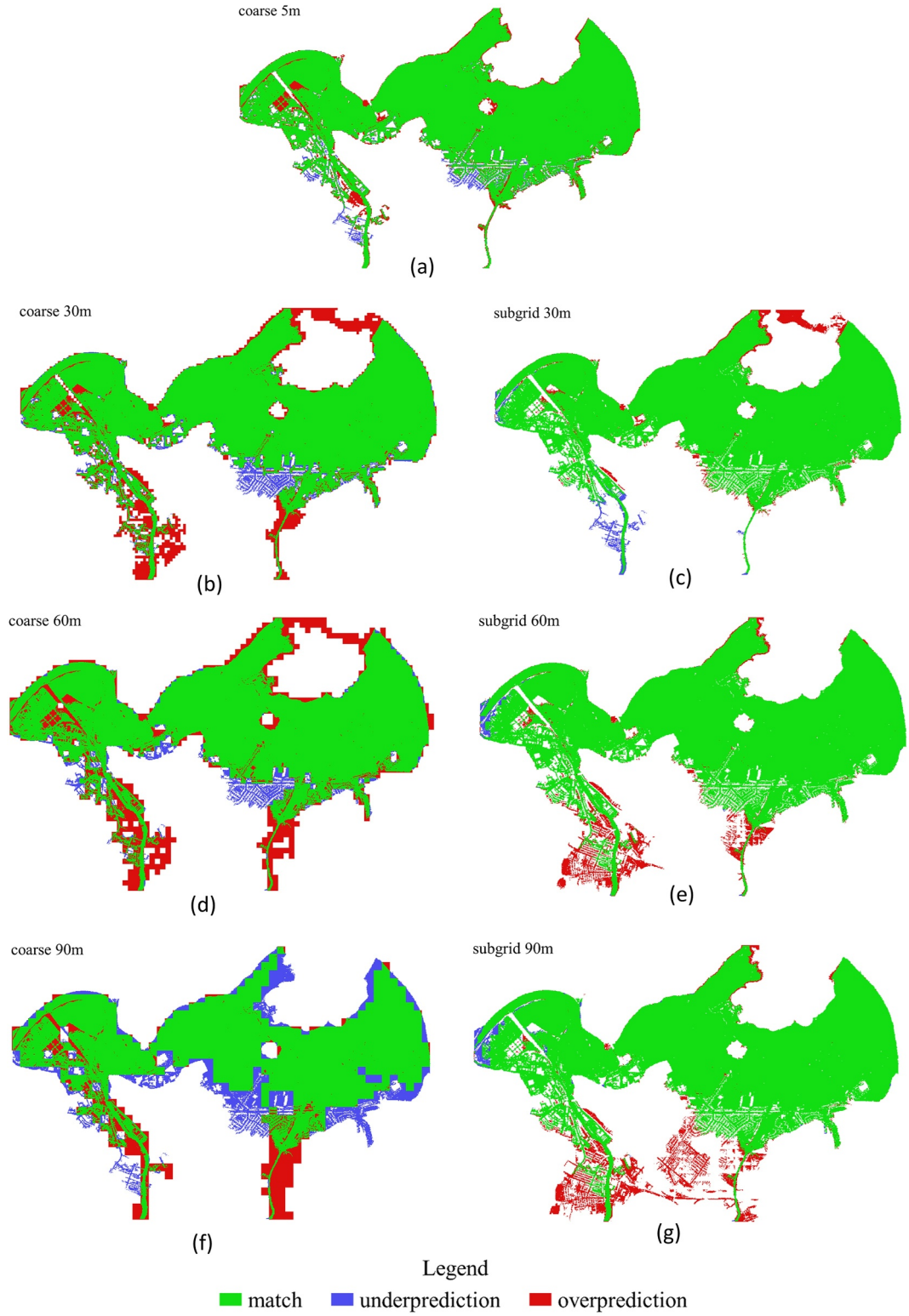

Figure 7. Comparison of the maximum inundation extents simulated by (a) coarse 5m, (b) coarse 30m, (c) subgrid 30m, (d) coarse 60m, (e) subgrid 30m, (f) coarse 90m, and (g) subgrid 90m with the extent simulated by HEC-RAS full 2D at 5 m.

19447973, 2024, 5, Downloaded from https://agupubs.onlinelibrary.wiley.com/doi/10.1029/2023WR035334 by Helmholtz-Zentrum Potsdam GFZ, Wiley Online Library on [14/05/2024]. See the Terms and Conditions (https://onlinelibrary.wiley.com/terms-and-conditions) on Wiley Online Library for rules of use; OA articles are governed by the applicable Creative Commons License

19447973, 2024, 5, Downloaded from https://agupubs.onlinelibrary.wiley.com/doi/10.1029/2023WR035334 by Helmholtz-Zentrum Potsdam GFZ, Wiley Online Library on [14/05/2024]. See the Terms and Conditions (https://onlinelibrary.wiley.com/terms-and-conditions) on Wiley Online Library for rules of use; OA articles are governed by the applicable Creative Commons License

model at 60 and 90 m grid sizes can be due to the fact that we tend to allocate the updated volume of water in a larger computational cell without being mindful of its distribution within the cell, though there can be variation in topography. This can only be captured using high-resolution DEM (e.g., HEC-RAS simulation on 5 m DEM) or the subgrid approach on a finer numerical grid (e.g., *subgrid* 30m setup). To sum up, the spatial flooding pattern in the urbanized area is well captured by the subgrid-inertial model, while the coarse-inertial model of similar grid size fails due to inaccurate representation of the within-grid topography.

The coarse-inertial model performs worse by exhibiting increased over and underprediction than the subgrid-inertial model. To a greater extent, it fails to simulate inundation along the roads, streets and highways. This is also reflected in the histogram depth distribution corresponding to over and underprediction areas. The plots are presented in Figure S3 of Supporting Information S2. The plots in Figure S3a of Supporting Information S2 show simulated depth distribution corresponding to coarse- and subgrid-inertial models in the case of overprediction. Figure S3b in Supporting Information S2 displays the depth values that were simulated by the reference HEC-RAS full2D but were not captured by the local-inertial models in the case of underprediction. The under-prediction of depths by the subgrid-inertial model is lesser in both values and counts. The *coarse* 5m setup reported an overpredicted area of 0.3 $km^{2,}$ and 90% of the overpredicted areas had depths within 1.2 m. For the 30 m grid size, the overpredicted area estimates of the coarse- and subgrid-inertial models are 0.83 and 0.2 km^2, respectively. The maximum inundation depth values for 90% of the overpredicted areas fall within 2.2 and 1.1 m, respectively, for *coarse* 30m and *subgrid* 30m setups. In the case of underprediction, the *coarse* 5m setup reported an area of 0.1 $km^{2,}$ and 90% of the underpredicted areas reported depths within 0.7 m. The underpredicted area is estimated to be around 0.3 and 0.1 km^2 for the *coarse* 30m and *subgrid* 30m, respectively. For the *coarse* 30m and *subgrid* 30m, the maximum inundation depth values for 90% of the underpredicted areas fall within 1.8 and 1.1 m, respectively. Thus, the subgrid-inertial model simulates not only lesser over and underpredicted areas but also the inundation depth values in these areas, which are of lesser magnitude compared to the coarse-inertial model of similar grid sizes.

To assess the ability of the local-inertial models to simulate maximum inundation extents, the fitness index (*F* index) (Bates et al., 2010; Kuiry et al., 2010) is estimated as follows,

$$F(\%) = \frac{A}{A + B + C} \times 100 \tag{16}$$

where *A* represents the areas that are wet in both the local-inertial and reference HEC-RAS full2D models' maximum inundation extents (i.e., match); *B* represents the areas that are dry in the local-inertial and wet in HEC-RAS full2D models' maximum inundation extents (i.e., underprediction); and *C* represents the areas that are wet in the local-inertial and dry in the HEC-RAS full2D models' maximum inundation extents (i.e., overprediction). The value varies from 0 to 1, with 1 representing a complete match. The *F* values for *coarse* 30m, *subgrid* 30m, *coarse* 60m, *subgrid* 60m, *coarse* 90m, and *subgrid* 90m are 81%, 94%, 78%, 92%, 72% and 89%, respectively. Hence, the fitness of inundation maps between the reference and subgrid-inertial model is always better compared to the coarse-inertial model at all grid resolutions. The accuracy metrics of all the model setups are further summarized in Tables 1 and 2. Table 1 lists the performance metrics of the local-inertial model for grid sizes 5 m up to 90 m to get an idea of where the subgrid-inertial model stands in terms of accuracy. Overall, from the plots showing inundation extents, maximum water level, depth time-series and performance metrics, it can be seen that the subgrid-inertial model with a 30 m grid size performs very close to the coarse-inertial and HEC-RAS models with the highest resolution of 5 m.

3.1.3. Computation Time Versus Accuracy

It is clear from the spider plots in Figure 8 that the coarse-inertial model does not result in similar accuracy to that of the subgrid-inertial model for all the considered grid resolutions. From the spider plots in Figure 8, it can be seen that even at a coarse grid size, implementation of the subgrid algorithm may result in a performance similar to that of a finer grid size. The coarse-inertial model is ~3.4 times faster than the subgrid-inertial model when the same resolution grid is used in the simulation. However, the optimal *subgrid* 30m model setup effectively simulates the flow along smaller terrain features like embankments, streets and roads in the urbanized flood plains of Carlisle city, while the coarse-inertial model at the same grid resolution fails to do so. The grid resolution for the coarse-inertial model is progressively refined to obtain an accuracy similar to that of the subgrid 30m. It is

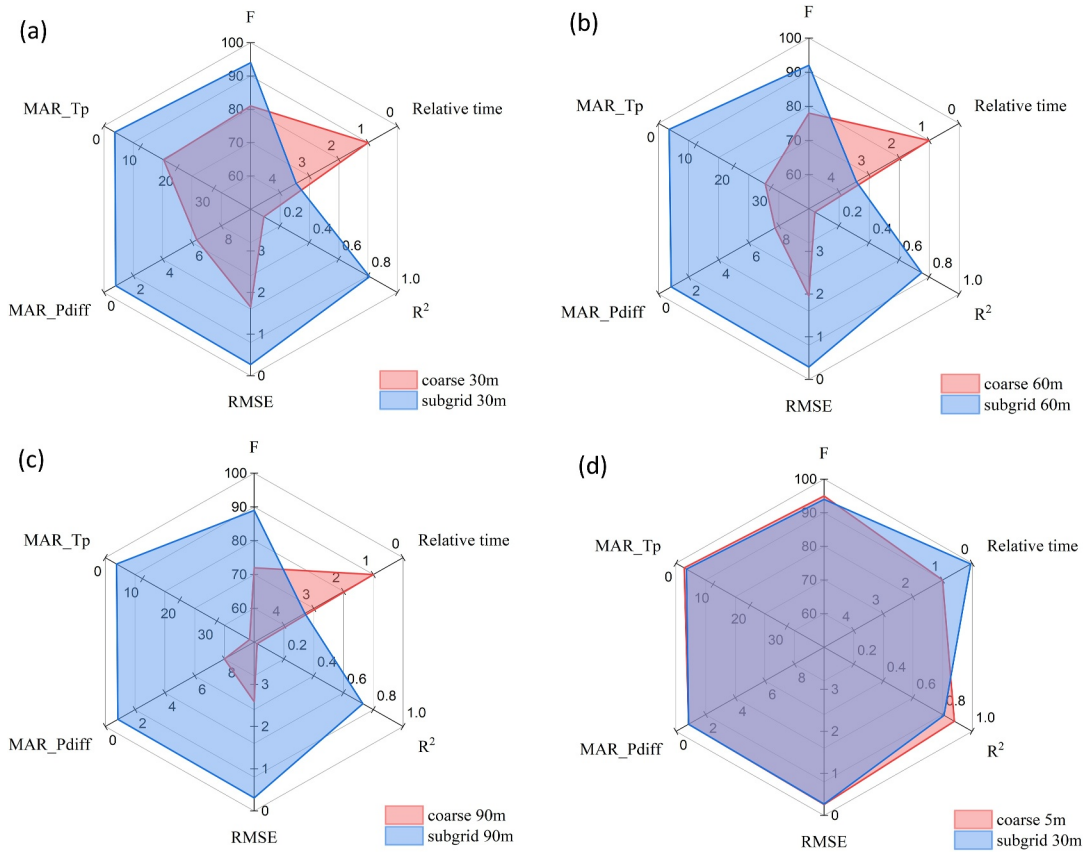

Figure 8. Spider plots showing various performance measures such as F (%), MAR_Tp (%), MAR_Pdiff (%), RMSE (m), and R^2 of coarse and subgrid models at (a) 30 m, (b) 60 m, (c) 90 m, and (d) coarse 5m and subgrid 30m respectively.

found that the coarse-inertial model in 5 m resolution maintains a similar level of accuracy to the subgrid-inertial 30 m setup and *HEC-RAS* 5m, as shown in Tables 1 and 2. The *HEC-RAS* 5m, *coarse* 5m and *subgrid* 30m are the three setups that are of similar accuracy and closer to the observed data. Among these three, the *subgrid* 30m is faster by ∼361 times and ∼21 times than that of *HEC-RAS* 5m and *coarse* 5m, respectively. The mass conservation error per time step as a percentage of volume in the domain (Bates & De Roo, 2000) were estimated for the coarse and subgrid-based inertial models. The *subgrid* 30m and *coarse* 30m reported mass error values of 0.13% and 0.21%, respectively. Therefore, when both accuracy and computational cost are to be optimized, the subgrid-inertial model wins against the coarse-inertial and HEC-RAS models in generating urban flood inundation in the subcritical flow regime. Nevertheless, the local-inertial models, in general, are significantly faster than the full 2D HEC-RAS model, offering a similar level of accuracy.

3.2. Urban Flooding of the Adyar River in Chennai City, India

The urban fluvial flooding of the Adyar River, which flows through Chennai city in the Indian state of Tamil Nadu, is taken as another application to illustrate the utility of the proposed subgrid-inertial model. The Adyar River basin experiences frequent flooding due to depressions and cyclonic disturbances during the northeast monsoon months of October, November, and December. The Adyar River runs through the Southern portion of the Chennai Metropolitan Area (CMA) before draining into the sea. A significant part of the city, under flooding risk due to the overflow from the Adyar River, is chosen as the hydraulic domain (Figure 9a). Apart from being a low-lying coastal city, the CMA is highly urbanized, with its riverbanks and flood plains, and water bodies being encroached upon. This, in turn, increases the vulnerability of the urbanized CMA and signifies the need for a computationally efficient high-resolution flood inundation mapping framework from flood forecasting and management perspectives. Apart from streets, highways, and buildings, the domain includes other smaller terrain features such as minor drains and canals. Hence, a Quick Bird DEM of 10 m × 10 m resolution is used as the base

19447973, 2024, 5, Downloaded from https://agupubs.onlinelibrary.wiley.com/doi/10.1029/2023WR035334 by Helmholtz-Zentrum Potsdam GFZ, Wiley Online Library on [14/05/2024]. See the Terms and Conditions (https://onlinelibrary.wiley.com/terms-and-conditions) on Wiley Online Library for rules of use; OA articles are governed by the applicable Creative Commons License

10.1029/2023WR035334

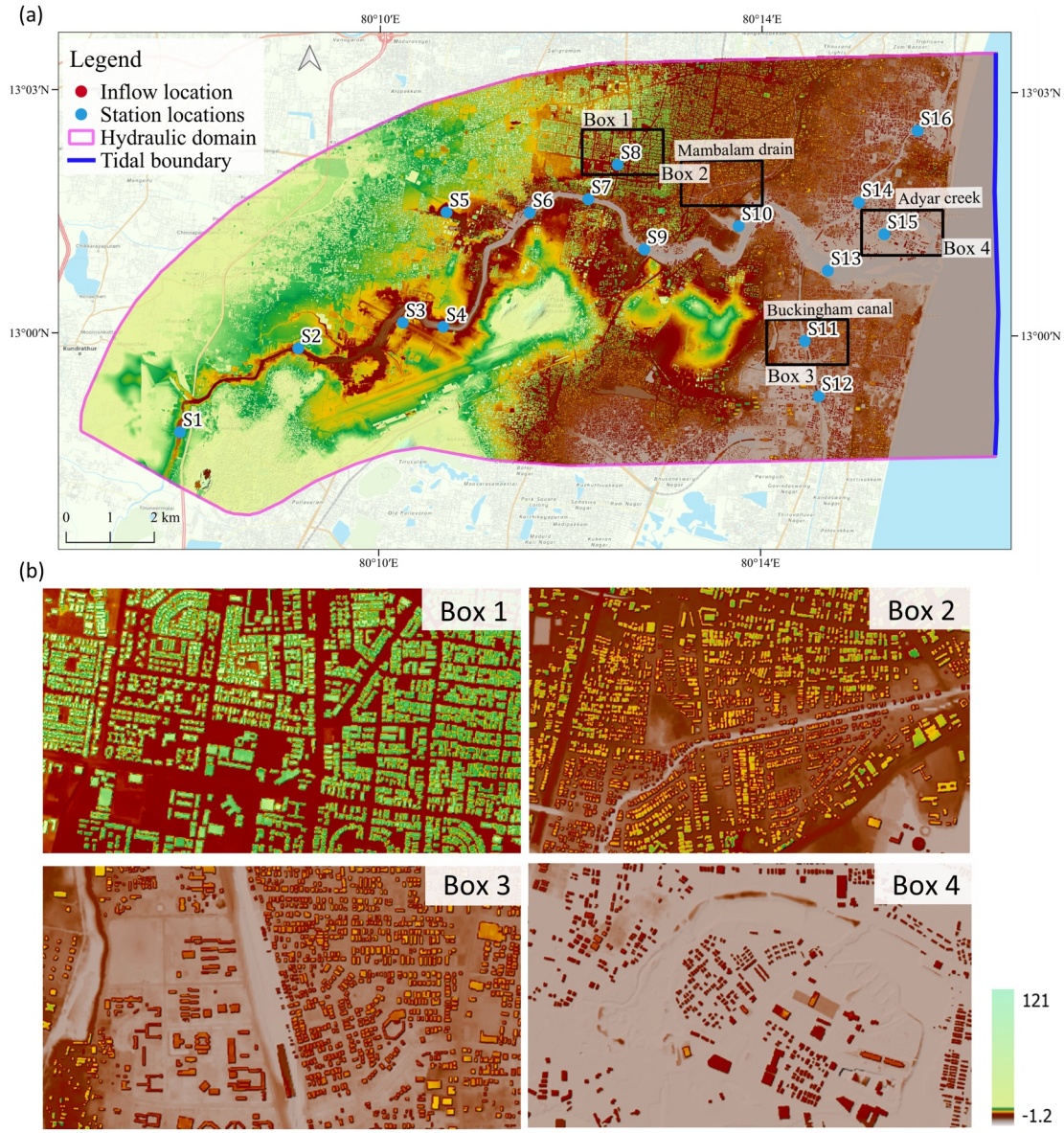

Figure 9. Adyar basin: (a) map of the study area with the observed locations and (b) zoomed-in views of the DEM of the study area. The boxes show small terrain features such as streets and buildings (Box 1), portions of Mambalam drain (Box 2), Buckingham canal (Box 3), and Adyar Creek (Box 4), respectively. The DEM is in the units of meters.

DEM, and the pixels corresponding to buildings were raised to a height of 6 m from the terrain. The complex topography of the DEM with smaller terrain features such as streets, buildings, Mambalam drain, Buckingham canal (~up to 60 m wide), and Adyar creek is shown enlarged in boxes in Figure 9. The 10 m resolution is not good enough for representing streets, small buildings, and other topographical features relevant to urban flood simulation and a finer resolution DEM makes the simulation intractable for flood forecasting purpose. However, a very high-resolution DEM (which is not available with the authors) can also be used in the developed model setup for emergency action planning under various hydro-meteorological scenarios. The extreme flooding event of 2015, spanning 80 hr, is chosen for the analysis herein. Nithila Devi et al. (2019) reported the calibration and validation of the hydrological model that was used to generate the river inflow into the hydraulic domain at the location indicated in Figure 9. A tidal boundary condition during the event is imposed downstream of the domain. Four numerical grid sizes of 10, 60, 90, and 120 m with r values of 1, 6, 9, and 12 are chosen for investigation. A Manning's n value of 0.035 $m^{-1/3}s$ is used in the study, as suggested by Ghosh et al. (2019) and Nithila Devi

19447973, 2024, 5, Downloaded from https://agupubs.onlinelibrary.wiley.com/doi/10.1029/2023WR035334 by Helmholtz-Zentrum Potsdam GFZ, Wiley Online Library on [14/05/2024]. See the Terms and Conditions (https://onlinelibrary.wiley.com/terms-and-conditions) on Wiley Online Library for rules of use; OA articles are governed by the applicable Creative Commons License

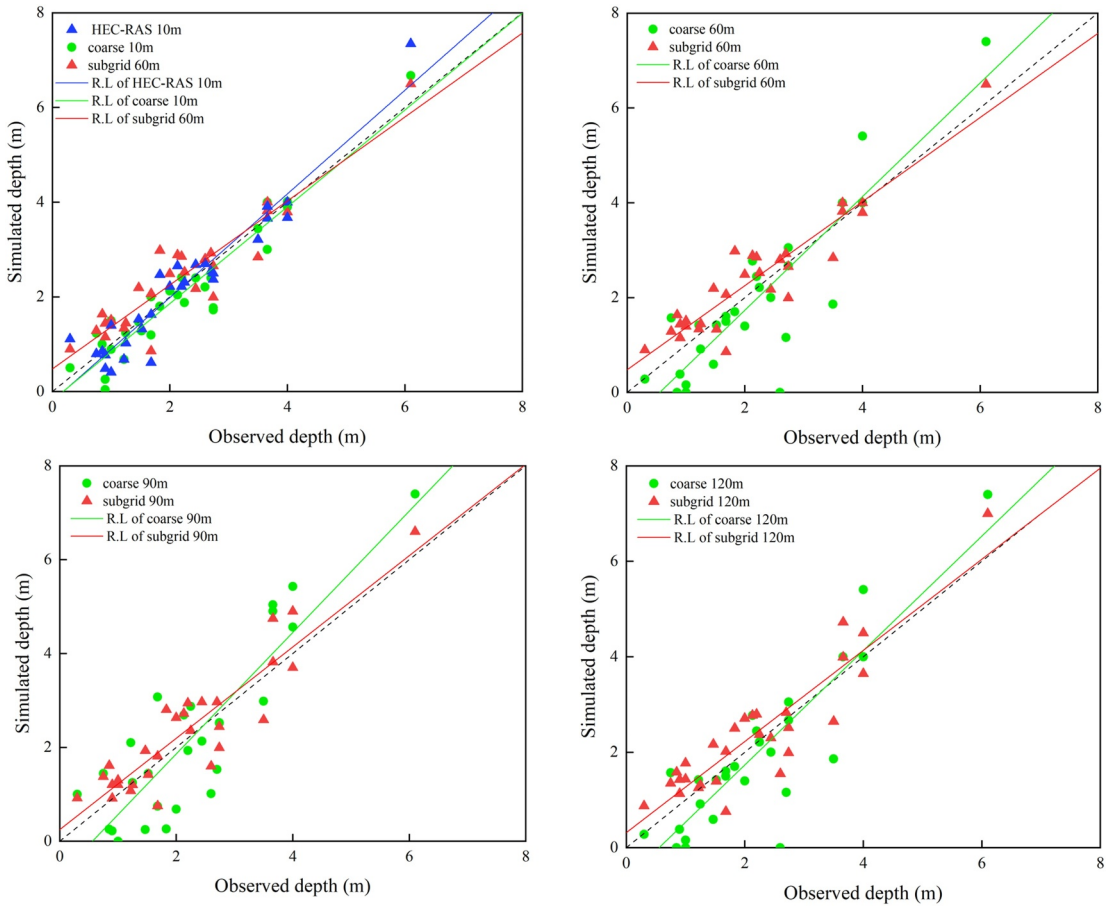

Figure 10. Scatter plots of observed and simulated maximum water depths for different models. R.L. corresponds to the regression line of the scatter.

et al. (2019). The flood event is also simulated using the *HEC-RAS full 2D* model with 10 m DEM input as a reference solution to assess the accuracy of the coarse- and subgrid-inertial models.

3.2.1. Comparison of Floodwater Marks and Time-Series of Water Levels

A post-flood survey of maximum floodwater marks was conducted for the 2015 flood event (Nithila Devi et al., 2019). The simulated maximum depths and observed floodwater marks at the surveyed locations are compared in Figure 10, and the R^2 and RMSE values are presented in Tables 3 and 4. As expected, *HEC-RAS* 10m has the highest accuracy with R^2 value of 0.91 and RMSE of 0.44 m. The spread of the subgrid-inertial model in all the 60 m, 90 m, and 120 m grids is closer to the 1:1 line than the coarse-inertial model. It should be noted that the *subgrid* 60m provides better accuracy among the subgrid-inertial model runs. It is evident from Tables 3 and 4 that the *subgrid* 60m setup can produce results with similar accuracy of *coarse* 10m and *HEC-RAS* 10m setups.

Time-series of water depths at various stations situated throughout the domain from the coarse- and subgrid-inertial models are compared with those from the *HEC-RAS* 10m further to assess the model accuracy (Figure 11). The hypothetical stations are located within the river (S1, S2, S4, S6, S7, S9, S13), on the floodplains (S3, S5, S8), and along the canals (Mambalam canal—S10; the southern portion of Buckingham canal—S11, S12; Adyar creek—S15; northern part of Buckingham canal—S14, S16) as marked in Figure 9. In all the stations, depth time-series from the subgrid-inertial model are closer to those from the reference *HEC-RAS* 10m, with *subgrid* 60m performing better at most of the stations. The coarse-inertial model fails to capture the within-grid bathymetry, so it does not simulate inundation over small terrain features on the flood plains. Figure 11 shows that only the subgrid-inertial model has reported inundation at stations S11, S12, S14, and S16, similar to the *HEC-RAS* 10m. While at stations S3, S5, and S8, the depth time-series of the coarse-inertial model deviates highly from the reference solutions, but the depth time-series of the subgrid-inertial model are closer to the reference solutions.

19447973, 2024, 5, Downloaded from https://agupubs.onlinelibrary.wiley.com/doi/10.1029/2023WR035334 by Helmholtz-Zentrum Potsdam GFZ, Wiley Online Library on [14/05/2024]. See the Terms and Conditions (https://onlinelibrary.wiley.com/terms-and-conditions) on Wiley Online Library for rules of use; OA articles are governed by the applicable Creative Commons License

19447973, 2024, 5, Downloaded from https://agupubs.onlinelibrary.wiley.com/doi/10.1029/2023WR035334 by Helmholtz-Zentrum Potsdam GFZ, Wiley Online Library on [14/05/2024]. See the Terms and Conditions (https://onlinelibrary.wiley.com/terms-and-conditions) on Wiley Online Library for rules of use; OA articles are governed by the applicable Creative Commons License

Table 3
Performance Metrics for Coarse Models of Different Grid Sizes up to 120 m

Model	R^2	RMSE (m)	MAR_Pdiff (%)	MAR_Tp (%)	F (%)	Time taken (s)	Relative time
HEC-RAS 10m	0.91	0.44	Ref.	Ref.	Ref.	232,199	659.7
coarse 10m	0.90	0.45	5.0	3.1	92	12,092	34.4
coarse 20m	0.89	0.45	14.2	7.9	91	1,812	5.2
coarse 30m	0.86	0.51	19.7	11.7	90	556	1.6
coarse 40m	0.84	0.57	20.5	12.3	89	246	0.7
coarse 50m	0.82	0.73	24.3	18.4	81	144	0.4
coarse 60m	0.80	0.86	29.6	20.3	77	114	0.3
coarse 70m	0.79	0.88	31.2	22.1	77	82	0.2
coarse 80m	0.79	0.91	33.8	24.8	76	66	0.2
coarse 90m	0.78	0.95	36.4	27.3	76	55	0.2
coarse 100m	0.77	0.97	38	27.6	75	49	0.1
coarse 110m	0.75	1.01	38.2	27.6	74	37	0.1
coarse 120m	0.73	1.02	40.6	27.9	73	31	0.1

Unlike the previous application, the time-series of water depths for the Adyar basin by all the model setups do not show much variation due to the error in gauge elevations in the aggregated grids. The reason can be attributed to the relatively flat terrain of the coastal region of the Adyar basin.

The MAR_Tp and MAR_Pdiff are calculated based on the time to peak and peak inundation depth differences between the local-inertial and the *HEC-RAS* 10m model setups at the 16 stations and summarized in Tables 3 and 4. The R^2 and RMSE values are estimated for the scatter of simulated and observed maximum water depths (Figure 10) at the post-flood survey locations. It has to be reiterated that the 16 stations are well distributed in the domain, located on the river and floodplains along canals and streets that are smaller terrain or within grid features. The MAR_Pdiff and MAR_Tp values of *subgrid* 60m are 5.3% and 3.2%, respectively, while those of the *coarse* 60m are 29.6% and 20.3%, respectively. Thus, it can be concluded that the *subgrid* 60m setup is very effective in simulating flooding along small terrain features present on the flood plains, similar to the *HEC-RAS* 10m model setup.

3.2.2. Comparison of Maximum Inundation Extent

During the Chennai floods in 2015, the maximum inundation map could not be captured by satellite imageries due to cloud cover. Figure 12 presents the maximum inundation extents of the coarse- and subgrid-inertial and HEC-RAS simulations. Qualitatively, the simulated maximum flood extent from the subgrid-inertial model, especially *subgrid* 60m, matches better with that from the *HEC-RAS* 10m. The enlarged extents shown in the boxes reiterate the ability of the subgrid-inertial model to capture flooding along roads, streets, minor drains, highways, and canals.

The maximum inundation extents from coarse- and subgrid-inertial models are further compared with that from the reference *HEC-RAS* 10m model setup, and the pixels corresponding to correct, under, and overprediction are shown in Figure 13. It can be seen from the difference maps in Figure 13 that the subgrid-inertial model can simulate flood inundation extents on a large domain reasonably similar to HEC-RAS model. The *F* values for

Table 4
Performance Metrics for Various Subgrid Models

Model	R^2	RMSE (m)	MAR_Pdiff (%)	MAR_Tp (%)	F (%)	Time taken (s)	Relative time
subgrid 60m	0.89	0.49	5.3	3.2	89	352	1
subgrid 90m	0.83	0.59	8.2	3.3	85	128	0.36
subgrid 120m	0.82	0.61	14.7	3.9	84	75	0.21

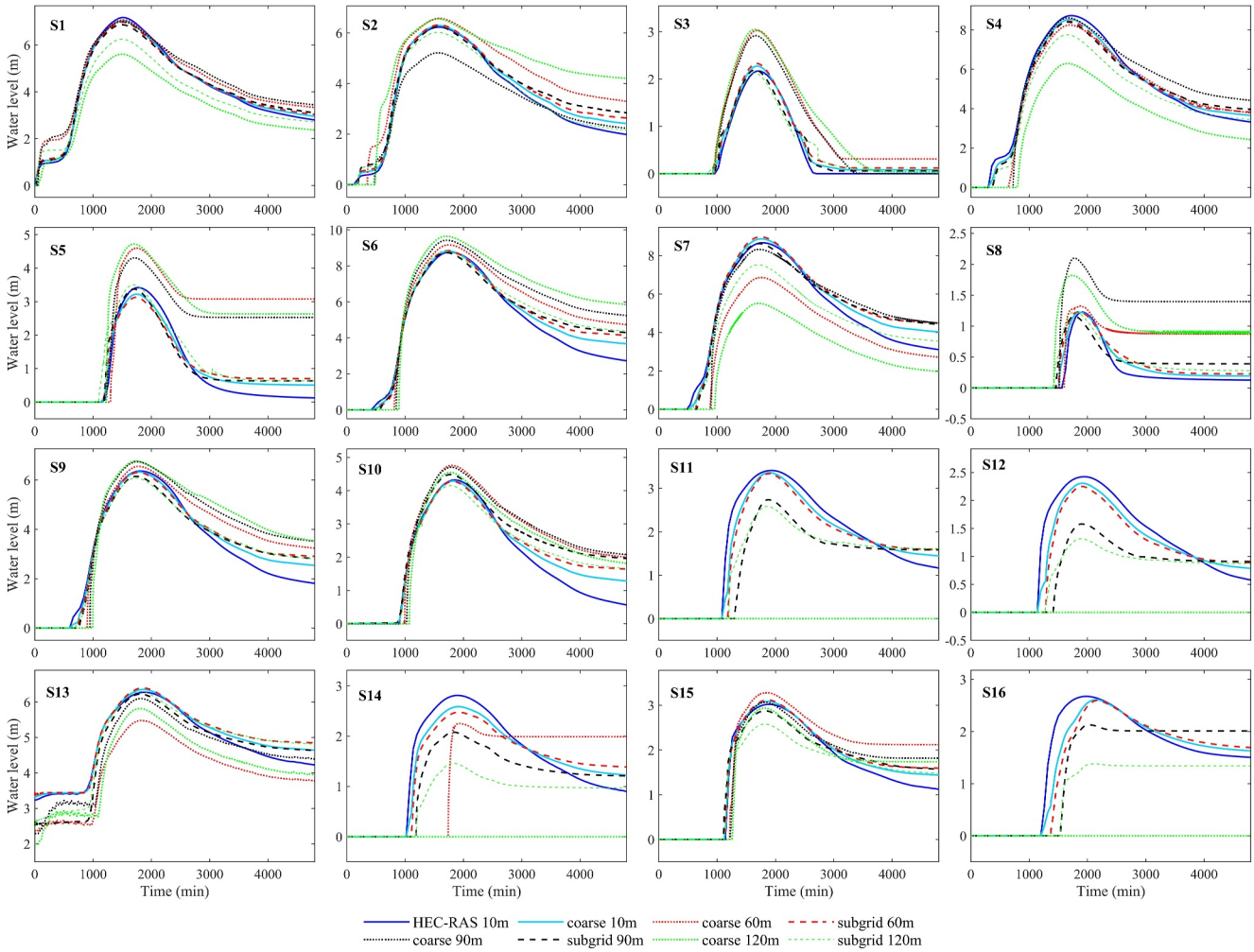

Figure 11. Depth time series of various models at the 16 stations.

subgrid 60m and *coarse* 60m are 89% and 77%, respectively. The *F* values for *subgrid* 90m, *coarse* 90m, *subgrid* 120m, and *coarse* 120m are 85%, 76%, 84%, and 73%, respectively. Also, Tables 3 and 4 summarize the *F* values for all the model setups. Thus, from the depth time-series and maximum inundation extents (Figures 11–13), it can be seen that the subgrid-inertial model can effectively resolve small terrain features and simulate inundation along canals such as the Mambalam drain, Buckingham canal, and highways. In particular, the *subgrid* 60m can also simulate urban flooding close to the *HEC-RAS* 10m setup. Hence, the fitness of inundation maps between the reference and subgrid-inertial model is always better compared to the coarse-inertial model at all grid resolutions. The accuracy metrics of all the model setups are further summarized in Tables 3 and 4. From Tables 3 and 4, it can be concluded that the *coarse* 10m setup can produce a similar level of accuracy to that of *subgrid* 60m and *HEC-RAS* 10m setups.

Figure S4 in Supporting Information S2 shows the histograms of the distribution of depth values of over and underpredicted areas corresponding to the coarse- and subgrid-inertial models. The subgrid-inertial model shows a noticeably lower underprediction than the coarse-inertial model of the same grid size. With the increase in grid size, though there is a visible increase in overprediction for the subgrid-inertial model, a significant decrease in the underprediction counteracts the simulation inaccuracy. In the case of a *coarse* 10m setup, the under and over-predicted areas are 2.6 and 2 km^2, respectively. For example, the area estimates of under and overprediction are 2.1 and 5 km^2, respectively, for the *subgrid* 60m setup. On the other hand, for the *coarse* 60m, the under and overpredicted areas are 5.7 and 4.1 km^2, respectively. 90% of the inundation depths fall within 0.9 and 0.5 m for over and underpredicted areas for the *coarse* 10m setup. In the case of *coarse* 60m and *subgrid* 60m setups, 90%

19447973, 2024, 5, Downloaded from https://agupubs.onlinelibrary.wiley.com/doi/10.1029/2023WR035334 by Helmholtz-Zentrum Potsdam GFZ, Wiley Online Library on [14/05/2024]. See the Terms and Conditions (https://onlinelibrary.wiley.com/terms-and-conditions) on Wiley Online Library for rules of use; OA articles are governed by the applicable Creative Commons License

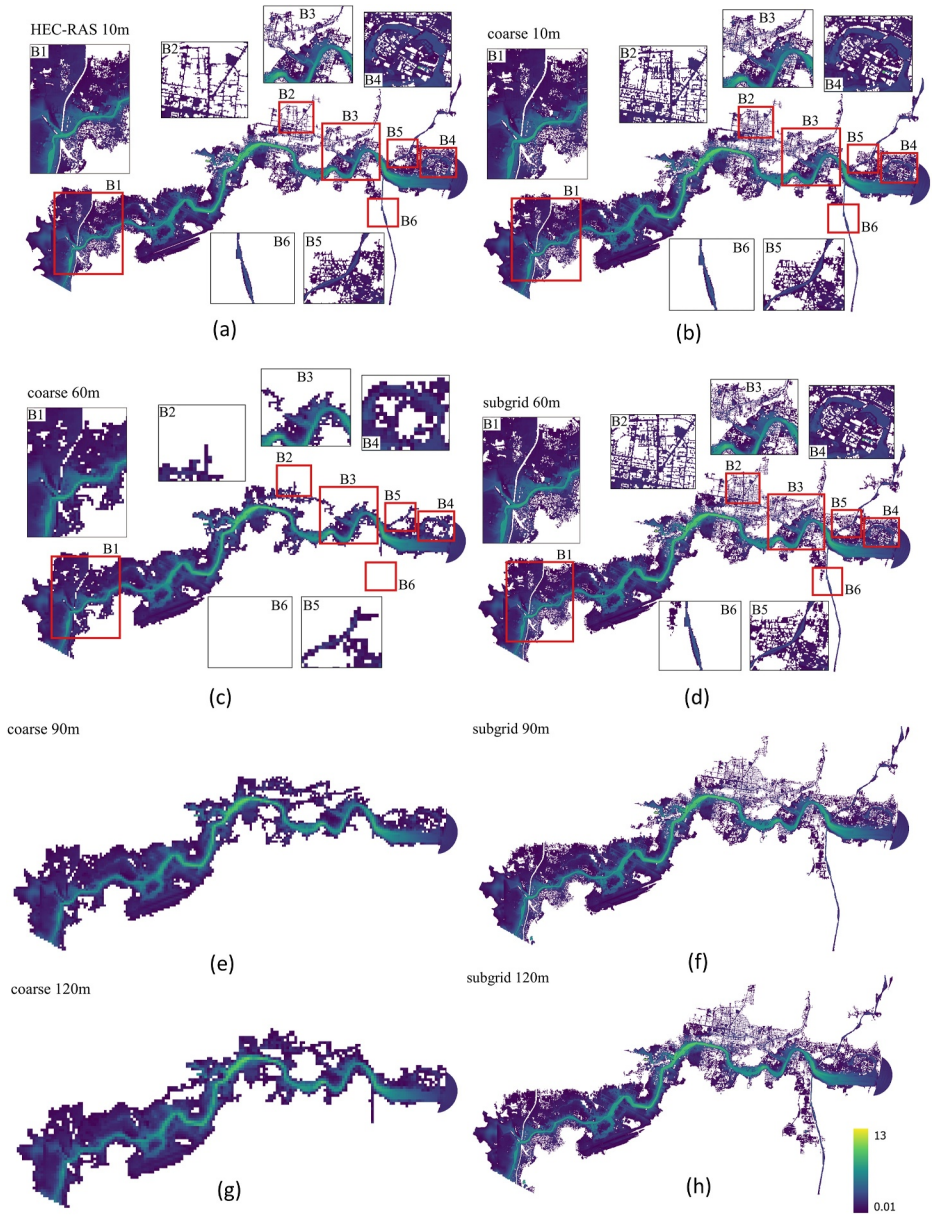

Figure 12. Maximum inundation extents simulated by the (a) HEC-RAS 10m, (b) coarse 10m, (c) coarse 60m, (d) subgrid 60m, (e) coarse 90m, (f) subgrid 90m, (g) coarse 120m, and (h) subgrid 120m. For the HEC full2D 10m, coarse 10m, subgrid 60m, and coarse 60m zoomed views of the smaller terrain features, such as highway (B1), streets (B2), Mambalam drain (B3), northern (B5), and southern Buckingham (B6) canals and Adyar creek (B4) are presented. The legend shows inundation depth in meters.

of the inundation depths fall within 1.8 and 1.2 m for the underpredicted areas. In the case of overpredicted areas, for *coarse* 60m and *subgrid* 60m, 90% of the inundation depths fall within 2 and 1.3 m, respectively. Overall, the over and underpredicted depth values for the subgrid-inertial model are relatively lower than that of the coarse-inertial model of the same grid size. Therefore, the proposed subgrid-inertial model performs better than the coarse-inertial model as far as flow depth and inundation extents are concerned.

3.2.3. Computation Time Versus Accuracy

The spider plots (Figure 14) clearly show that for the coarse-inertial model, with an increase in grid coarsening from 60 to 120 m, the performance measures drop to a greater degree than in the subgrid-inertial model. Tables 3

19447973, 2024, 5, Downloaded from https://agupubs.onlinelibrary.wiley.com/doi/10.1029/2023WR035334 by Helmholtz-Zentrum Potsdam GFZ, Wiley Online Library on [14/05/2024]. See the Terms and Conditions (https://onlinelibrary.wiley.com/terms-and-conditions) on Wiley Online Library for rules of use; OA articles are governed by the applicable Creative Commons License

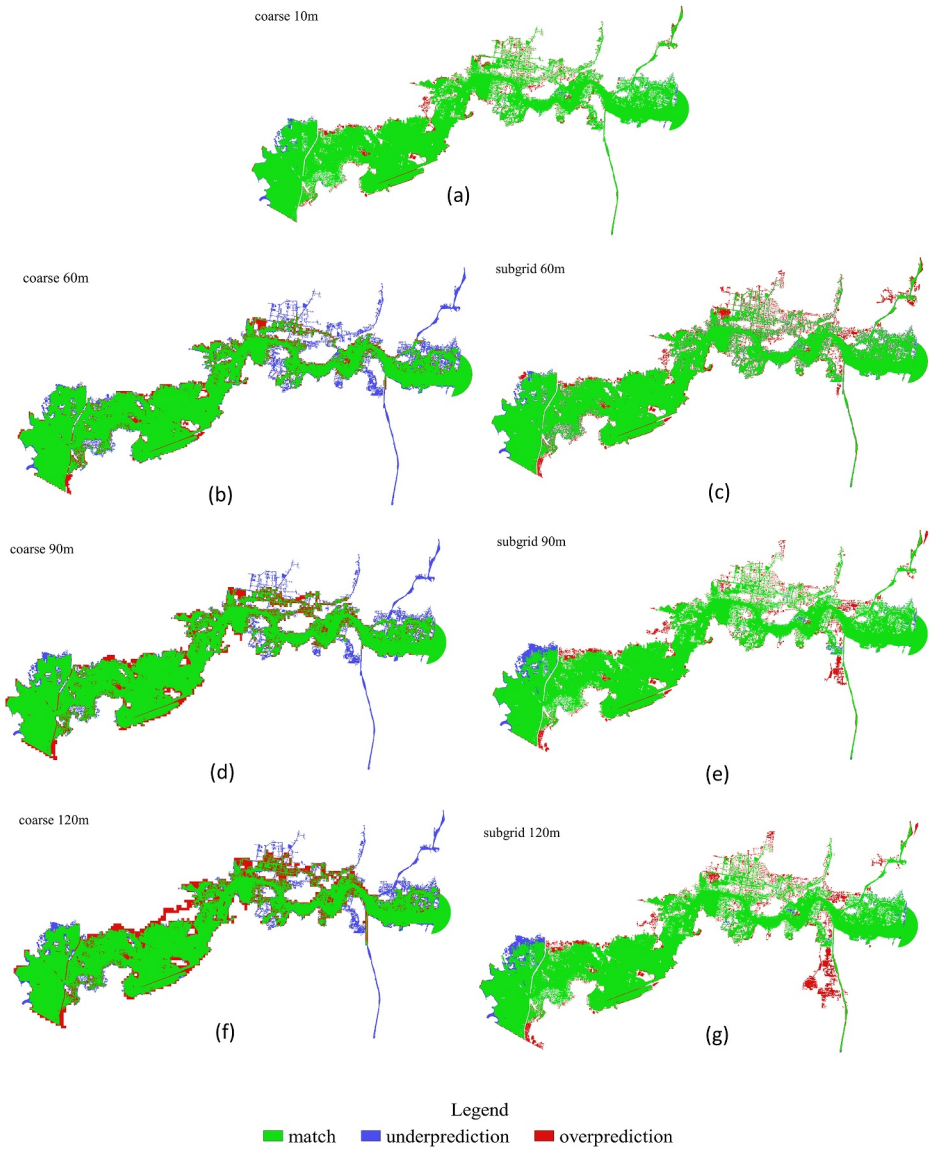

Figure 13. Comparison of the maximum inundation extents simulated by (a) coarse 10m, (b) coarse 60m, (c) subgrid 60m, (d) coarse 90m, (e) subgrid 90m, (f) coarse 120m, and (g) subgrid 120m with the extent simulated by HEC-RAS full 2D at 10 m.

and 4 show that the subgrid-inertial model is significantly more accurate than the coarse-inertial model of the same grid size at a higher computation cost (~2.4–3.5 times). Like the Carlisle flooding case, the proposed subgrid algorithm on coarser grids results in a performance similar to that of a finer grid coarse-inertial model (Sridharan et al., 2020). The subgrid-inertial model on a 60 m grid shows almost similar performance as that of the 10 m grid size coarse-inertial model but at ~34 times lesser computation time. However, at 60 m grid size, the coarse-inertial model, though around ~3 times faster than the subgrid-inertial model, doesn't capture urban flood inundation dynamics, that is, it fails to simulate inundation along smaller terrain features in the urbanized floodplains. Thus, it can be concluded that the grid size of the coarse-inertial model needs to be refined considerably to attain a similar level of accuracy to that of the subgrid-inertial model. As a result, the computational advantage of the coarse-inertial model over the subgrid-inertial model of the same grid size is compensated for by the accuracy offered by the subgrid-inertial model. It also needs to be noted that the subgrid-inertial model on a 60 m grid performs close to that of the HEC-RAS model on the fine grid of 10 m resolution at ~660 times faster computation time while successfully capturing the flood dynamics. In other words, out of the

19447973, 2024, 5, Downloaded from https://agupubs.onlinelibrary.wiley.com/doi/10.1029/2023WR035334 by Helmholtz-Zentrum Potsdam GFZ, Wiley Online Library on [14/05/2024]. See the Terms and Conditions (https://onlinelibrary.wiley.com/terms-and-conditions) on Wiley Online Library for rules of use; OA articles are governed by the applicable Creative Commons License

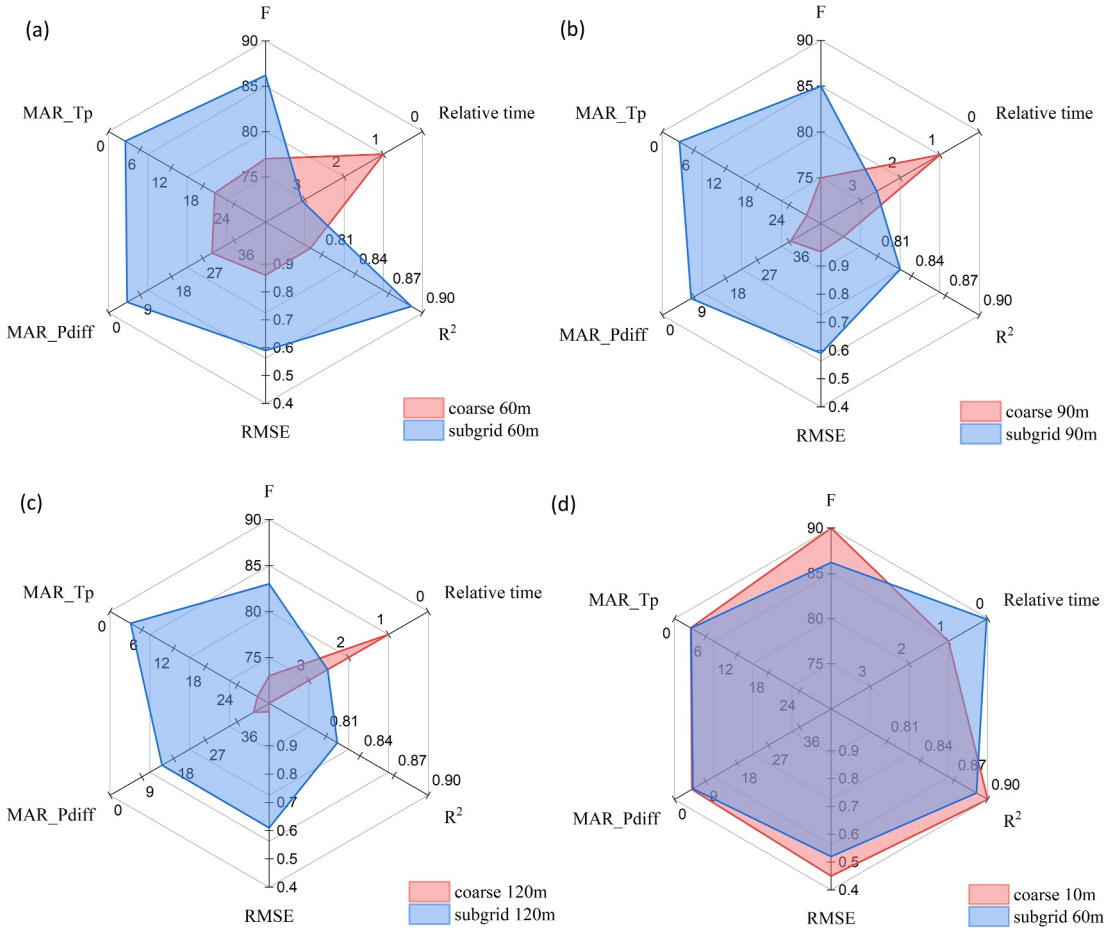

Figure 14. Spider plots showing various performance measures such as F (%), MAR_Tp (%), MAR_Pdiff (%), RMSE (m), and R^2 of coarse and subgrid models at (a) 60 m, (b) 90 m, (c) 120 m, and (d) coarse 10m and subgrid 60m, respectively.

model setups that provide higher accuracy, namely *HEC-RAS* 10m, *coarse* 10m, and *subgrid* 60m, the *subgrid* 60m is the fastest and hence, the advantage of the subgrid-inertial model can be appreciated in simulating computationally efficient flood inundation resolving street-level urban features. Also, it has to be mentioned that the mass conservation error values for the *subgrid* 60m and *coarse* 60m are 0.15% and 0.23%, respectively.

4. Conclusions

A subgrid-based local-inertial model is developed to simulate the effect of the complex urbanized terrain on the flood dynamics while using a large numerical grid. The subgrid within the coarse numerical grid defines the high-resolution topographic data which can describe urban features. The model stores relationships of wetted volume and face area with water surface elevation for the high-resolution subgrid-scale landscape a priori in a preprocessing step. While executing the solution steps of the local-inertial SWEs, the pre-stored relationships are used to dynamically vary the wetted face area based on the water surface elevation in the momentum equation and then update the water surface elevation based on the estimated wetted volume in the continuity equation. The proposed model is tested on idealized channels of different sinuosity, flooding of rivers with their floodplains comprising moderately and highly urbanized cities, namely, Carlisle in the UK and Chennai in Tamil Nadu, India. High-resolution bathymetry data from LiDAR and Quick Bird are used for the real-world flooding applications in Carlisle and Chennai cities, respectively. The simulations from the proposed model and naive grid-averaged coarse-inertial model (i.e., traditional local-inertial model) of large grid size are compared with those from the high-resolution full 2D model (HEC-RAS) and limited observed data. The subgrid-inertial model consistently performs better than the coarse-inertial model for various grid sizes. The proposed model can resolve flow depths around several fine-resolution urban features such as streets, roads, highways, major

19447973, 2024, 5, Downloaded from https://agupubs.onlinelibrary.wiley.com/doi/10.1029/2023WR035334 by Helmholtz-Zentrum Potsdam GFZ, Wiley Online Library on [14/05/2024]. See the Terms and Conditions (https://onlinelibrary.wiley.com/terms-and-conditions) on Wiley Online Library for rules of use; OA articles are governed by the applicable Creative Commons License

19447973, 2024, 5, Downloaded from https://agupubs.onlinelibrary.wiley.com/doi/10.1029/2023WR035334 by Helmholtz-Zentrum Potsdam GFZ, Wiley Online Library on [14/05/2024]. See the Terms and Conditions (https://onlinelibrary.wiley.com/terms-and-conditions) on Wiley Online Library for rules of use; OA articles are governed by the applicable Creative Commons License

canals, drains, etc. At the same time, the coarse-inertial model of the same grid size cannot simulate flooding accurately as the details are lost due to simple averaging of the within-grid topography. In the Carlisle case study, it is seen that the subgrid-inertial model of a 30 m grid produces results with similar accuracy as that of the coarse-inertial model of a 5 m grid. Similarly, in the Chennai case study, it is seen that the subgrid-inertial model of the 60 m grid maintains accuracy similar to that of the coarse-inertial 10 m grid. In both cases, the subgrid-inertial model is found to be ∼21 and ∼34 times faster than the coarse-inertial model for achieving a similar level of accuracy. However, the subgrid-inertial model is ∼361 and ∼660 times faster than the HEC-RAS model for the Carlisle and Chennai flood studies, respectively. Consequently, out of the models that operate at large grid sizes, the proposed subgrid-inertial model is more accurate than the existing local-inertial model.

The specific conclusions from the study are summarized as follows:

1. The model can run on a larger grid size while still representing the within-grid topography but at a higher computation cost (∼2.5–3.9) than the traditional local-inertial model (e.g., LISFLOOD-FP) for the same grid size. Nonetheless, for a similar accuracy, the subgrid-inertial model is faster (∼21–34 times) than the coarse-inertial model. It should be noted that using the subgrid-inertial model at a large grid size is computationally efficient than the high-resolution full 2D HEC-RAS model, as the latter is around ∼361 to 660 times costlier for the test cases.
2. The proposed subgrid-inertial model effectively resolves small-scale urban features like canals, streets, roads, highways, etc., where the existing coarse grid models fall short. The proposed model is developed with the focus on generating computationally efficient inundation extent and flood depth forecasts resolving street-level features rather than building-by-building level, using a coarse grid and limited computational facilities. For the proposed model, the mass conservation errors were 0.15% and 0.13% for the real-world test cases: Chennai and Carlisle cities, respectively.
3. To attain a level of accuracy comparable to that reported by the proposed subgrid model, the existing local-inertial model requires a finer grid, thereby increasing the model run time. In other words, the proposed model is an advancement over the existing local-inertial models, as it improves the accuracy of the flood depth simulation without resorting to grid refinement. Further, the preprocessing steps in the proposed model also don't need much technical expertise as opposed to the existing porosity-based approaches, thus allowing for wider usage by the flood management community to avert loss of lives and properties.
4. In simulating the maximum inundation extent for the Chennai city test case, the coarse-inertial model with final reprojection step, coarse-inertial model that uses only subgrid-wetted volume and the proposed subgrid-inertial model (both subgrid-wetted volume and face area) are 1%, 2%, and 12% more accurate than the existing coarse-inertial model, respectively at the same grid size of 60 m. This shows that the subgrid representation of the coarse grid interfaces chiefly improves mass flux and volume computations and makes the proposed subgrid-inertial model more accurate than the coarse-inertial model that has even included a reprojection step.

For these reasons, the proposed subgrid-inertial model can be considered a viable solution in real-time forecasting, monitoring and managing slow-rising floods in highly populated cities, especially in the Global South, with limited computing facilities.

Conflict of Interest

The authors declare no conflicts of interest relevant to this study.

Data Availability Statement

All the data sets used in the test cases (Nithila Devi & Kuiry, 2023) are available at Zenodo via https://doi.org/10.5281/zenodo.7699784, last accessed in April 2024.

Acknowledgments
This work was funded by the Department of Science and Technology, India, under the SPLICE–Climate Change Programme (Grant DST/CCP/CoE/141/2018C) and Asia-Pacific Network (APN) under its Collaborative Regional Research Programme (CRRP) (Grant CRRP2022-08MY-Sarangi). The authors would like to acknowledge Dr. B. Sridharan, Department of Civil Engineering, IIT Indore, India, for his support at various stages of the paper. The authors would like to thank Prof. Paul D. Bates, School of Geographical Sciences, Cabot Institute for the Environment, University of Bristol for his suggestions that led them to add relevant literature and interesting discussions, thereby improving the manuscript. The authors also thank him for providing the necessary DEM, flow, and flood data of the 2005 Carlisle flooding event. The authors are also grateful to the editor and the anonymous reviewer for helping us improve the manuscript.

References

Ahmadisharaf, E., & Kalyanapu, A. J. (2019). A coupled probabilistic hydrologic and hydraulic modelling framework to investigate the uncertainty of flood loss estimates. *Journal of Flood Risk Management*, *12*(S2), e12536. https://doi.org/10.1111/jfr3.12536

Ahmadisharaf, E., Kalyanapu, A. J., & Chung, E. S. (2016). Spatial probabilistic multi-criteria decision making for assessment of flood management alternatives. *Journal of Hydrology*, *533*, 365–378. https://doi.org/10.1016/j.jhydrol.2015.12.031

Apel, H., Vorogushyn, S., & Merz, B. (2022). Brief communication: Impact forecasting could substantially improve the emergency management of deadly floods: Case study July 2021 floods in Germany. *Natural Hazards and Earth System Sciences*, *22*(9), 3005–3014. https://doi.org/10.5194/NHESS-22-3005-2022

Aronica, G., Bates, P. D., & Horritt, M. S. (2002). Assessing the uncertainty in distributed model predictions using observed binary pattern information within GLUE. *Hydrological Processes*, *16*(10), 2001–2016. https://doi.org/10.1002/HYP.398

Aronica, G. T., Franza, F., Bates, P. D., & Neal, J. C. (2012). Probabilistic evaluation of flood hazard in urban areas using Monte Carlo simulation. *Hydrological Processes*, *26*(26), 3962–3972. https://doi.org/10.1002/hyp.8370

Barthélémy, S., Ricci, S., Rochoux, M. C., Le Pape, E., & Thual, O. (2017). Ensemble-based data assimilation for operational flood forecasting – On the merits of state estimation for 1D hydrodynamic forecasting through the example of the "Adour Maritime" river. *Journal of Hydrology*, *552*, 210–224. https://doi.org/10.1016/j.jhydrol.2017.06.017

Bates, P. D., & De Roo, A. P. J. (2000). A simple raster-based model for flood inundation simulation. *Journal of Hydrology*, *236*(1–2), 54–77. https://doi.org/10.1016/S0022-1694(00)00278-X

Bates, P. D., Horritt, M. S., & Fewtrell, T. J. (2010). A simple inertial formulation of the shallow water equations for efficient two-dimensional flood inundation modelling. *Journal of Hydrology*, *387*(1–2), 33–45. https://doi.org/10.1016/j.jhydrol.2010.03.027

Bates, P. D., Marks, K. J., & Horritt, M. S. (2003). Optimal use of high-resolution topographic data in flood inundation models. *Hydrological Processes*, *17*(3), 537–557. https://doi.org/10.1002/hyp.1113

Benkhaldoun, F., Elmahi, I., Moumna, A., & Seaid, M. (2016). A non-homogeneous Riemann solver for shallow water equations in porous media. *Applicable Analysis*, *95*(10), 2181–2202. https://doi.org/10.1080/00036811.2015.1067304

Bhuyian, M. N. M., Kalyanapu, A. J., & Nardi, F. (2015). Approach to digital elevation model correction by improving channel conveyance. *Journal of Hydrologic Engineering*, *20*(5), 4014062. https://doi.org/10.1061/(asce)he.1943-5584.0001020

Brown, J. D., Spencer, T., & Moeller, I. (2007). Modeling storm surge flooding of an urban area with particular reference to modeling uncertainties: A case study of Canvey Island, United Kingdom. *Water Resources Research*, *43*(6), W06402. https://doi.org/10.1029/2005WR004597

Bruwier, M., Archambeau, P., Erpicum, S., Pirotton, M., & Dewals, B. (2017). Shallow-water models with anisotropic porosity and merging for flood modelling on Cartesian grids. *Journal of Hydrology*, *554*, 693–709. https://doi.org/10.1016/J.JHYDROL.2017.09.051

Canestrelli, A., Fagherazzi, S., & Lanzoni, S. (2012). A mass-conservative centered finite volume model for solving two-dimensional two-layer shallow water equations for fluid mud propagation over varying topography and dry areas. *Advances in Water Resources*, *40*, 54–70. https://doi.org/10.1016/J.ADVWATRES.2012.01.009

Casas, A., Riaño, D., Greenberg, J., & Ustin, S. (2012). Assessing levee stability with geometric parameters derived from airborne LiDAR. *Remote Sensing of Environment*, *117*, 281–288. https://doi.org/10.1016/J.RSE.2011.10.003

Casulli, V. (2009). A high-resolution wetting and drying algorithm for free-surface hydrodynamics. *International Journal for Numerical Methods in Fluids*, *60*(4), 391–408. https://doi.org/10.1002/fld.1896

Casulli, V., & Stelling, G. S. (2011). Semi-implicit subgrid modelling of three-dimensional free-surface flows. *International Journal for Numerical Methods in Fluids*, *67*(4), 441–449. https://doi.org/10.1002/fld.2361

Cea, L., & Vázquez-Cendón, M. E. (2010). Unstructured finite volume discretization of two-dimensional depth-averaged shallow water equations with porosity. *International Journal for Numerical Methods in Fluids*, *63*(8), 903–930. https://doi.org/10.1002/FLD.2107

Chen, A. S., Evans, B., Djordjević, S., & Savić, D. A. (2012a). A coarse-grid approach to representing building blockage effects in 2D urban flood modelling. *Journal of Hydrology*, *426–427*, 1–16. https://doi.org/10.1016/J.JHYDROL.2012.01.007

Chen, A. S., Evans, B., Djordjević, S., & Savić, D. A. (2012b). Multi-layered coarse grid modelling in 2D urban flood simulations. *Journal of Hydrology*, *470–471*, 1–11. https://doi.org/10.1016/J.JHYDROL.2012.06.022

Cloke, H. L., & Pappenberger, F. (2009). Ensemble flood forecasting: A review. *Journal of Hydrology*, *375*(3–4), 613–626. https://doi.org/10.1016/j.jhydrol.2009.06.005

Coulthard, T. J., Neal, J. C., Bates, P. D., Ramirez, J., de Almeida, G. A. M., & Hancock, G. R. (2013). Integrating the LISFLOOD-FP 2D hydrodynamic model with the CAESAR model: Implications for modelling landscape evolution. *Earth Surface Processes and Landforms*, *38*(15), 1897–1906. https://doi.org/10.1002/esp.3478

Courty, L. G., Pedrozo-Acuña, A., & Bates, P. D. (2017). Itzï (version 17.1): An open-source, distributed GIS model for dynamic flood simulation. *Geoscientific Model Development*, *10*(4), 1835–1847. https://doi.org/10.5194/gmd-10-1835-2017

Dazzi, S., Shustikova, I., Domeneghetti, A., Castellarin, A., & Vacondio, R. (2021). Comparison of two modelling strategies for 2D large-scale flood simulations. *Environmental Modelling & Software*, *146*, 105225. https://doi.org/10.1016/J.ENVSOFT.2021.105225

De Almeida, G. A. M., & Bates, P. (2013). Applicability of the local inertial approximation of the shallow water equations to flood modeling. *Water Resources Research*, *49*(8), 4833–4844. https://doi.org/10.1002/wrcr.20366

De Almeida, G. A. M., Bates, P., Freer, J. E., & Souvignet, M. (2012). Improving the stability of a simple formulation of the shallow water equations for 2-D flood modeling. *Water Resources Research*, *48*(5), W05528. https://doi.org/10.1029/2011WR011570

Defina, A. (2000). Two-dimensional shallow flow equations for partially dry areas. *Water Resources Research*, *36*(11), 3251–3264. https://doi.org/10.1029/2000WR900167

Defina, A., D'alpaos, L., & Matticchio, B. (1994). A new set of equations for very shallow water and partially dry areas suitable to 2D numerical models. In *Modelling of flood propagation over initially dry areas* (pp. 72–81).

De Paiva, R. C. D., Buarque, D. C., Collischonn, W., Bonnet, M. P., Frappart, F., Calmant, S., & Bulhões Mendes, C. A. (2013). Large-scale hydrologic and hydrodynamic modeling of the Amazon River basin. *Water Resources Research*, *49*(3), 1226–1243. https://doi.org/10.1002/wrcr.20067

Devitt, L., Neal, J., Coxon, G., Savage, J., & Wagener, T. (2023). Flood hazard potential reveals global floodplain settlement patterns. *Nature Communications*, *14*(1), 2801. https://doi.org/10.1038/S41467-023-38297-9

Di Baldassarre, G., Schumann, G., Bates, P. D., Freer, J. E., & Beven, K. J. (2010). Cartographie de zone inondable: Un examen critique d'approches déterministe et probabiliste. *Hydrological Sciences Journal*, *55*(3), 364–376. https://doi.org/10.1080/02626661003683389

Dottori, F., Di Baldassarre, G., & Todini, E. (2013). Detailed data is welcome, but with a pinch of salt: Accuracy, precision, and uncertainty in flood inundation modeling. *Water Resources Research*, *49*(9), 6079–6085. https://doi.org/10.1002/WRCR.20406

Dottori, F., Salamon, P., Bianchi, A., Alfieri, L., Hirpa, F. A., & Feyen, L. (2016). Development and evaluation of a framework for global flood hazard mapping. *Advances in Water Resources*, *94*, 87–102. https://doi.org/10.1016/j.advwatres.2016.05.002

Dottori, F., & Todini, E. (2010). A 2D flood inundation model based on cellular automata approach. In *XVIII International Conference on Water Resources CMWR*.

Falter, D., Vorogushyn, S., Lhomme, J., Apel, H., Gouldby, B., & Merz, B. (2013). Hydraulic model evaluation for large-scale flood risk assessments. *Hydrological Processes*, *27*(9), 1331–1340. https://doi.org/10.1002/HYP.9553

19447973, 2024, 5, Downloaded from https://agupubs.onlinelibrary.wiley.com/doi/10.1029/2023WR035334 by Helmholtz-Zentrum Potsdam GFZ, Wiley Online Library on [14/05/2024]. See the Terms and Conditions (https://onlinelibrary.wiley.com/terms-and-conditions) on Wiley Online Library for rules of use; OA articles are governed by the applicable Creative Commons License

Fernández-Pato, J., & García-Navarro, P. (2016). 2D zero-inertia model for solution of overland flow problems in flexible meshes. *Journal of Hydrologic Engineering*, *21*(11), 4016038. https://doi.org/10.1061/(ASCE)HE.1943-5584.0001428
Ferrari, A., Viero, D. P., Vacondio, R., Defina, A., & Mignosa, P. (2019). Flood inundation modeling in urbanized areas: A mesh-independent porosity approach with anisotropic friction. *Advances in Water Resources*, *125*, 98–113. https://doi.org/10.1016/J.ADVWATRES.2019.01.010
Fewtrell, T., Bates, P., de Wit, A., Asselman, N., & Sayers, P. (2008). Comparison of varying complexity numerical models for the prediction of flood inundation in Greenwich, UK.
Ghosh, S., Karmakar, S., Saha, A., Mohanty, M. P., Ali, S., Raju, S. K., et al. (2019). Development of India's first integrated expert urban flood forecasting system for Chennai. *Current Science*, *117*(5), 741–745.
Guidolin, M., Chen, A. S., Ghimire, B., Keedwell, E. C., Djordjević, S., & Savić, D. A. (2016). A weighted cellular automata 2D inundation model for rapid flood analysis. *Environmental Modelling & Software*, *84*, 378–394. https://doi.org/10.1016/j.envsoft.2016.07.008
Guinot, V. (2012). Multiple porosity shallow water models for macroscopic modelling of urban floods. *Advances in Water Resources*, *37*, 40–72. https://doi.org/10.1016/J.ADVWATRES.2011.11.002
Guinot, V. (2017a). A critical assessment of flux and source term closures in shallow water models with porosity for urban flood simulations. *Advances in Water Resources*, *109*, 133–157. https://doi.org/10.1016/J.ADVWATRES.2017.09.002
Guinot, V. (2017b). Consistency and bicharacteristic analysis of integral porosity shallow water models. Explaining model oversensitivity to mesh design. *Advances in Water Resources*, *107*, 43–55. https://doi.org/10.1016/j.advwatres.2017.06.008
Guinot, V., Sanders, B. F., & Schubert, J. E. (2017). Dual integral porosity shallow water model for urban flood modelling. *Advances in Water Resources*, *103*, 16–31. https://doi.org/10.1016/j.advwatres.2017.02.009
Guinot, V., & Soares-Frazão, S. (2006). Flux and source term discretization in two-dimensional shallow water models with porosity on unstructured grids. *International Journal for Numerical Methods in Fluids*, *50*(3), 309–345. https://doi.org/10.1002/FLD.1059
Hodges, B. R. (2015). Representing hydrodynamically important blocking features in coastal or riverine lidar topography. *Natural Hazards and Earth System Sciences*, *15*(5), 1011–1023. https://doi.org/10.5194/nhess-15-1011-2015
Horritt, M. S., & Bates, P. D. (2001). Predicting floodplain inundation: Raster-based modelling versus the finite-element approach. *Hydrological Processes*, *15*(5), 825–842. https://doi.org/10.1002/hyp.188
Horritt, M. S., Bates, P. D., Fewtrell, T. J., Mason, D. C., & Wilson, M. D. (2010). Modelling the hydraulics of the Carlisle 2005 flood event. *Proceedings of the Institution of Civil Engineers: Water Management*, *163*(6), 273–281. https://doi.org/10.1680/WAMA.2010.163.6.273/ASSET/IMAGES/SMALL/WAMA163-273-F6.GIF
Hunter, N. M., Bates, P. D., Horritt, M. S., & Wilson, M. D. (2006). Improved simulation of flood flows using storage cell models. *Proceedings of the Institution of Civil Engineers - Water Management*, *159*(1), 9–18. https://doi.org/10.1680/wama.2006.159.1.9
Ivanov, V. Y., Xu, D., Dwelle, M. C., Sargsyan, K., Wright, D. B., Katopodes, N., et al. (2021). Breaking down the computational barriers to real-time urban flood forecasting. *Geophysical Research Letters*, *48*(20), e2021GL093585. https://doi.org/10.1029/2021GL093585
Jordi, A., Georgas, N., Blumberg, A., Yin, L., Chen, Z., Wang, Y., et al. (2019). A next-generation coastal ocean operational system: Probabilistic flood forecasting at street scale. *Bulletin of the American Meteorological Society*, *100*(1), 41–54. https://doi.org/10.1175/BAMS-D-17-0309.1
Kalyanapu, A. J., Shankar, S., Pardyjak, E. R., Judi, D. R., & Burian, S. J. (2011). Assessment of GPU computational enhancement to a 2D flood model. *Environmental Modelling & Software*, *26*(8), 1009–1016. https://doi.org/10.1016/j.envsoft.2011.02.014
Kuiry, S. N., Sen, D., & Bates, P. D. (2010). Coupled 1D–Quasi-2D flood inundation model with unstructured grids. *Journal of Hydraulic Engineering*, *136*(8), 493–506. https://doi.org/10.1061/(asce)hy.1943-7900.0000211
Lamb, R., Crossley, M., & Waller, S. (2009). A fast two-dimensional floodplain inundation model. *Proceedings of the Institution of Civil Engineers: Water Management*, *162*(6), 363–370. https://doi.org/10.1680/wama.2009.162.6.363
Leandro, J., Chen, A. S., Djordjević, S., & Savić, D. A. (2009). Comparison of 1D/1D and 1D/2D coupled (Sewer/Surface) hydraulic models for urban flood simulation. *Journal of Hydraulic Engineering*, *135*(6), 495–504. https://doi.org/10.1061/(ASCE)HY.1943-7900.0000037
Leitão, J. P., Simões, N. E., Maksimović, Č., Ferreira, F., Prodanović, D., Matos, J. S., & Sá Marques, A. (2010). Real-time forecasting urban drainage models: Full or simplified networks? *Water Science and Technology*, *62*(9), 2106–2114. https://doi.org/10.2166/WST.2010.382
Lewis, M., Bates, P., Horsburgh, K., Neal, J., & Schumann, G. (2013). A storm surge inundation model of the northern Bay of Bengal using publicly available data. *Quarterly Journal of the Royal Meteorological Society*, *139*(671), 358–369. https://doi.org/10.1002/QJ.2040
Li, Z., & Hodges, B. R. (2019). Modeling subgrid-scale topographic effects on shallow marsh hydrodynamics and salinity transport. *Advances in Water Resources*, *129*, 1–15. https://doi.org/10.1016/j.advwatres.2019.05.004
Liang, Q., Xia, X., & Hou, J. (2015). Efficient urban flood simulation using a GPU-accelerated SPH model. *Environmental Earth Sciences*, *74*(11), 7285–7294. https://doi.org/10.1007/S12665-015-4753-4/TABLES/2
Liu, Y., & Pender, G. (2013). Carlisle 2005 urban flood event simulation using cellular automata-based rapid flood spreading model. *Soft Computing*, *17*(1), 29–37. https://doi.org/10.1007/s00500-012-0898-1
Mason, D. C., Horritt, M. S., Hunter, N. M., & Bates, P. D. (2007). Use of fused airborne scanning laser altimetry and digital map data for urban flood modelling. *Hydrological Processes*, *21*(11), 1436–1447. https://doi.org/10.1002/HYP.6343
McMillan, H. K., & Brasington, J. (2007). Reduced complexity strategies for modelling urban floodplain inundation. *Geomorphology*, *90*(3–4), 226–243. https://doi.org/10.1016/J.GEOMORPH.2006.10.031
Meesuk, V., Vojinovic, Z., Mynett, A. E., & Abdullah, A. F. (2015). Urban flood modelling combining top-view LiDAR data with ground-view SfM observations. *Advances in Water Resources*, *75*, 105–117. https://doi.org/10.1016/J.ADVWATRES.2014.11.008
Merwade, V., Olivera, F., Arabi, M., & Edleman, S. (2008). Uncertainty in flood inundation mapping: Current issues and future directions. *Journal of Hydrologic Engineering*, *13*(7), 608–620. https://doi.org/10.1061/(ASCE)1084-0699(2008)13:7(608)
Ming, X., Liang, Q., Xia, X., Li, D., & Fowler, H. J. (2020). Real-time flood forecasting based on a high-performance 2-D hydrodynamic model and numerical weather predictions. *Water Resources Research*, *56*(7), e2019WR025583. https://doi.org/10.1029/2019WR025583
Neal, J., Fewtrell, T., & Trigg, M. (2009). Parallelisation of storage cell flood models using OpenMP. *Environmental Modelling and Software*, *24*(7), 872–877. https://doi.org/10.1016/j.envsoft.2008.12.004
Neal, J., Schumann, G., & Bates, P. (2012). A subgrid channel model for simulating river hydraulics and floodplain inundation over large and data sparse areas. *Water Resources Research*, *48*(11), 1–16. https://doi.org/10.1029/2012WR012514
Neal, J., Villanueva, I., Wright, N., Willis, T., Fewtrell, T., & Bates, P. (2012). How much physical complexity is needed to model flood inundation? *Hydrological Processes*, *26*(15), 2264–2282. https://doi.org/10.1002/HYP.8339
Neal, J. C., Bates, P. D., Fewtrell, T. J., Hunter, N. M., Wilson, M. D., & Horritt, M. S. (2009). Distributed whole city water level measurements from the Carlisle 2005 urban flood event and comparison with hydraulic model simulations. *Journal of Hydrology*, *368*(1–4), 42–55. https://doi.org/10.1016/j.jhydrol.2009.01.026
Neal, J. C., Fewtrell, T. J., Bates, P. D., & Wright, N. G. (2010). A comparison of three parallelisation methods for 2D flood inundation models. *Environmental Modelling & Software*, *25*(4), 398–411. https://doi.org/10.1016/J.ENVSOFT.2009.11.007

19447973, 2024, 5, Downloaded from https://agupubs.onlinelibrary.wiley.com/doi/10.1029/2023WR035334 by Helmholtz-Zentrum Potsdam GFZ, Wiley Online Library on [14/05/2024]. See the Terms and Conditions (https://onlinelibrary.wiley.com/terms-and-conditions) on Wiley Online Library for rules of use; OA articles are governed by the applicable Creative Commons License

Nithila Devi, N., & Kuiry, S. N. (2023). Datasets for subgrid-based local inertial model [Dataset]. *Zenodo*. https://doi.org/10.5281/zenodo.7699784

Nithila Devi, N., Sridharan, B., & Kuiry, S. N. (2019). Impact of urban sprawl on future flooding in Chennai city, India. *Journal of Hydrology*, *574*, 486–496. https://doi.org/10.1016/J.JHYDROL.2019.04.041

Ozdemir, H., & Akbas, A. (2023). Is there a consistency in basin morphometry and hydrodynamic modelling results in terms of the flood generation potential of basins? A case study from the Ulus River Basin (Türkiye). *Journal of Hydrology*, *625*, 129926. https://doi.org/10.1016/J.JHYDROL.2023.129926

Özgen, I., Zhao, J., Liang, D., & Hinkelmann, R. (2016). Urban flood modeling using shallow water equations with depth-dependent anisotropic porosity. *Journal of Hydrology*, *541*, 1165–1184. https://doi.org/10.1016/J.JHYDROL.2016.08.025

Pappenberger, F., Beven, K., Horritt, M., & Blazkova, S. (2005). Uncertainty in the calibration of effective roughness parameters in HEC-RAS using inundation and downstream level observations. *Journal of Hydrology*, *302*(1–4), 46–69. https://doi.org/10.1016/j.jhydrol.2004.06.036

Pappenberger, F., Beven, K. J., Hunter, N. M., Bates, P. D., Gouweleeuw, B. T., Thielen, J., & de Roo, A. P. J. (2005). Cascading model uncertainty from medium range weather forecasts (10 days) through a rainfall-runoff model to flood inundation predictions within the European Flood Forecasting System (EFFS). *Hydrology and Earth System Sciences*, *9*(4), 381–393. https://doi.org/10.5194/HESS-9-381-2005

Pau, J. C., & Sanders, B. F. (2006). Performance of parallel implementations of an explicit finite-volume shallow-water model. *Journal of Computing in Civil Engineering*, *20*(2), 99–110. https://doi.org/10.1061/(ASCE)0887-3801(2006)20:2(99)

Petaccia, G., Soares-Frazão, S., Savi, F., Natale, L., & Zech, Y. (2009). Simplified versus detailed two-dimensional approaches to transient flow modeling in urban areas. *Journal of Hydraulic Engineering*, *136*(4), 262–266. https://doi.org/10.1061/(ASCE)HY.1943-7900.0000154

Platzek, F. W., Stelling, G. S., Jankowski, J. A., Patzwahl, R., & Pietrzak, J. D. (2016). An efficient semi-implicit subgrid method for free-surface flows on hierarchical grids. *International Journal for Numerical Methods in Fluids*, *80*(12), 715–741. https://doi.org/10.1002/FLD.4172

Pontes, P. R. M., Fan, F. M., Fleischmann, A. S., de Paiva, R. C. D., Buarque, D. C., Siqueira, V. A., et al. (2017). MGB-IPH model for hydrological and hydraulic simulation of large floodplain river systems coupled with open source GIS. *Environmental Modelling and Software*, *94*, 1–20. https://doi.org/10.1016/j.envsoft.2017.03.029

Robson, A. J., Moore, R. J., Wells, S. C., Rudd, A., Mattingley, P. S., & Cole, S. J. (2016). Understanding the performance of flood forecasting models. *Science Report SC130006/R2*.

Rong, Y., Bates, P., & Neal, J. (2022). An improved subgrid channel model with upwind form artificial diffusion for river hydrodynamics and floodplain inundation simulation. *Geoscientific Model Development Discussions*, *2022*, 1–31. https://doi.org/10.5194/gmd-2022-234

Sampson, C. C., Fewtrell, T. J., Duncan, A., Shaad, K., Horritt, M. S., & Bates, P. D. (2012). Use of terrestrial laser scanning data to drive decimetric resolution urban inundation models. *Advances in Water Resources*, *41*, 1–17. https://doi.org/10.1016/J.ADVWATRES.2012.02.010

Sanders, B. F., & Schubert, J. E. (2019). PRIMo: Parallel raster inundation model. *Advances in Water Resources*, *126*, 79–95. https://doi.org/10.1016/J.ADVWATRES.2019.02.007

Sanders, B. F., Schubert, J. E., & Detwiler, R. L. (2010). ParBreZo: A parallel, unstructured grid, Godunov-type, shallow-water code for high-resolution flood inundation modeling at the regional scale. *Advances in Water Resources*, *33*(12), 1456–1467. https://doi.org/10.1016/J.ADVWATRES.2010.07.007

Sanders, B. F., Schubert, J. E., & Gallegos, H. A. (2008). Integral formulation of shallow-water equations with anisotropic porosity for urban flood modeling. *Journal of Hydrology*, *362*(1–2), 19–38. https://doi.org/10.1016/j.jhydrol.2008.08.009

Sanders, B. F., Schubert, J. E., Kahl, D. T., Mach, K. J., Brady, D., AghaKouchak, A., et al. (2022). Large and inequitable flood risks in Los Angeles, California. *Nature Sustainability*, *6*(1), 47–57. https://doi.org/10.1038/s41893-022-00977-7

Sanyal, J., Carbonneau, P., & Densmore, A. L. (2013). Hydraulic routing of extreme floods in a large ungauged river and the estimation of associated uncertainties: A case study of the Damodar River, India. *Natural Hazards*, *66*(2), 1153–1177. https://doi.org/10.1007/S11069-012-0540-7/FIGURES/17

Savage, J. T. S., Bates, P., Freer, J., Neal, J., & Aronica, G. (2016). When does spatial resolution become spurious in probabilistic flood inundation predictions? *Hydrological Processes*, *30*(13), 2014–2032. https://doi.org/10.1002/HYP.10749

Schubert, J. E., Luke, A., AghaKouchak, A., & Sanders, B. F. (2022). A Framework for mechanistic flood inundation forecasting at the metropolitan scale. *Water Resources Research*, *58*(10), e2021WR031279. https://doi.org/10.1029/2021WR031279

Sehili, A., Lang, G., Lippert, C., Sehili, A., & Lang, G. (2014). High-resolution subgrid models: Background, grid generation, and implementation. *Ocean Dynamics*, *64*(4), 519–535. https://doi.org/10.1007/s10236-014-0693-x

Shaw, J., Kesserwani, G., Neal, J., Bates, P., & Sharifian, M. K. (2021). LISFLOOD-FP 8.0: The new discontinuous Galerkin shallow-water solver for multi-core CPUs and GPUs. *Geoscientific Model Development*, *14*(6), 3577–3602. https://doi.org/10.5194/GMD-14-3577-2021

Shustikova, I., Domeneghetti, A., Neal, J. C., Bates, P., & Castellarin, A. (2019). Comparing 2D capabilities of HEC-RAS and LISFLOOD-FP on complex topography. *Hydrological Sciences Journal*, *64*(14), 1769–1782. https://doi.org/10.1080/02626667.2019.1671982

Smeeckaert, J., Mallet, C., David, N., Chehata, N., & Ferraz, A. (2013). Large-scale classification of water areas using airborne topographic lidar data. *Remote Sensing of Environment*, *138*, 134–148. https://doi.org/10.1016/J.RSE.2013.07.004

Smemoe, C. M., Nelson, E. J., Zundel, A. K., Woodruff Miller, A., & Woodruff, A. (2007). Demonstrating flood-plain uncertainty using flood probability maps. *Journal of the American Water Resources Association*, *43*(2), 359–371. https://doi.org/10.1111/j.1752-1688.2007.00028.x

Soares-Frazão, S., Lhomme, J., Guinot, V., & Zech, Y. (2008). Two-dimensional shallow-water model with porosity for urban flood modelling. *Journal of Hydraulic Research*, *46*(1), 45–64. https://doi.org/10.1080/00221686.2008.9521842

Sridharan, B., Bates, P. D., Sen, D., & Kuiry, S. N. (2021). Local-inertial shallow water model on unstructured triangular grids. *Advances in Water Resources*, *152*, 103930. https://doi.org/10.1016/J.ADVWATRES.2021.103930

Sridharan, B., Gurivindapalli, D., Kuiry, S. N., Mali, V. K., Nithila Devi, N., Bates, P. D., & Sen, D. (2020). Explicit expression of weighting factor for improved estimation of numerical flux in local inertial models. *Water Resources Research*, *56*(7), e2020WR027357. https://doi.org/10.1029/2020WR027357

Stelling, G. S. (2012). Quadtree flood simulations with sub-grid digital elevation models. *Proceedings of the Institution of Civil Engineers - Water Management*, *165*(10), 567–580. https://doi.org/10.1680/wama.12.00018

Stephens, T. A., & Bledsoe, B. P. (2020). Probabilistic mapping of flood hazards: Depicting uncertainty in streamflow, land use, and geomorphic adjustment. *Anthropocene*, *29*, 100231. https://doi.org/10.1016/j.ancene.2019.100231

Su, B., Huang, H., & Zhu, W. (2019). An urban pluvial flood simulation model based on diffusive wave approximation of shallow water equations. *Hydrology Research*, *50*(1), 138–154. https://doi.org/10.2166/NH.2017.233

Thielen, J., Bartholmes, J., Ramos, M.-H., & De Roo, A. (2009). The European Flood Alert System-Part 1: Concept and development. *Hydrology and Earth System Sciences*, *13*(2), 125–140. https://doi.org/10.5194/hess-13-125-2009

Try, S., Lee, G., Yu, W., Oeurng, C., & Jang, C. (2018). Large-scale flood-inundation modeling in the Mekong River Basin. *Journal of Hydrologic Engineering*, *23*(7), 5018011. https://doi.org/10.1061/(ASCE)HE.1943-5584.0001664

19447973, 2024, 5, Downloaded from https://agupubs.onlinelibrary.wiley.com/doi/10.1029/2023WR035334 by Helmholtz-Zentrum Potsdam GFZ, Wiley Online Library on [14/05/2024]. See the Terms and Conditions (https://onlinelibrary.wiley.com/terms-and-conditions) on Wiley Online Library for rules of use; OA articles are governed by the applicable Creative Commons License

USACE. (2016). Hydrologic Modeling System System HEC-HMS, user's manual version 4.2. Retrieved from https://www.hec.usace.army.mil/software/hec-hms/documentation/HEC-HMS_Users_Manual_4.2.pdf

Velickovic, M., Zech, Y., Soares-Frazão, S., Professor, E., & Soares-frazão, S. (2017). Steady-flow experiments in urban areas and anisotropic porosity model. *Journal of Hydraulic Research*, *55*(1), 85–100. https://doi.org/10.1080/00221686.2016.1238013

Viero, D. P. (2019). Modelling urban floods using a finite element staggered scheme with an anisotropic dual porosity model. *Journal of Hydrology*, *568*, 247–259. https://doi.org/10.1016/J.JHYDROL.2018.10.055

Viero, D. P., & Valipour, M. (2017). Modeling anisotropy in free-surface overland and shallow inundation flows. *Advances in Water Resources*, *104*, 1–14. https://doi.org/10.1016/j.advwatres.2017.03.007

Volp, N. D., Van Prooijen, B. C., & Stelling, G. S. (2013). A finite volume approach for shallow water flow accounting for high-resolution bathymetry and roughness data. *Water Resources Research*, *49*(7), 4126–4135. https://doi.org/10.1002/WRCR.20324

Wang, C. K., & Philpot, W. D. (2007). Using airborne bathymetric lidar to detect bottom type variation in shallow waters. *Remote Sensing of Environment*, *106*(1), 123–135. https://doi.org/10.1016/J.RSE.2006.08.003

Wasko, C., & Sharma, A. (2015). Steeper temporal distribution of rain intensity at higher temperatures within Australian storms. *Nature Geoscience*, *8*(7), 527–529. https://doi.org/10.1038/ngeo2456

Wing, O. E. J., Bates, P. D., Sampson, C. C., Smith, A. M., Johnson, K. A., & Erickson, T. A. (2017). Validation of a 30 m resolution flood hazard model of the conterminous United States. *Water Resources Research*, *53*(9), 7968–7986. https://doi.org/10.1002/2017WR020917

Wing, O. E. J., Sampson, C. C., Bates, P. D., Quinn, N., Smith, A. M., & Neal, J. C. (2019). A flood inundation forecast of Hurricane Harvey using a continental-scale 2D hydrodynamic model. *Journal of Hydrology X*, *4*, 100039. https://doi.org/10.1016/J.HYDROA.2019.100039

Wu, G., Shi, F., Kirby, J. T., Mieras, R., Liang, B., Li, H., & Shi, J. (2016). A pre-storage, subgrid model for simulating flooding and draining processes in salt marshes. *Coastal Engineering*, *108*, 65–78. https://doi.org/10.1016/j.coastaleng.2015.11.008

Wu, W., Emerton, R., Duan, Q., Wood, A. W., Wetterhall, F., & Robertson, D. E. (2020). Ensemble flood forecasting: Current status and future opportunities. *WIREs Water*, *7*(3). https://doi.org/10.1002/wat2.1432

Wuebbles, D. J., Easterling, D. R., Hayhoe, K., Knutson, T., Kopp, R. E., Kossin, J. P., et al. (2017). In D. J. Wuebbles, D. W. Fahey, K. A. Hibbard, D. J. Dokken, B. C. Stewart, & T. K. Maycock (Eds.), *Chapter 1: Our globally Changing Climate. Climate Science Special Report: Fourth National Climate Assessment* (Vol. 1). https://doi.org/10.7930/J08S4N35

Yamazaki, D., De Almeida, G. A. M., & Bates, P. D. (2013). Improving computational efficiency in global river models by implementing the local inertial flow equation and a vector-based river network map. *Water Resources Research*, *49*(11), 7221–7235. https://doi.org/10.1002/wrcr.20552

Yamazaki, D., Kanae, S., Kim, H., & Oki, T. (2011). A physically based description of floodplain inundation dynamics in a global river routing model. *Water Resources Research*, *47*(4), 1–21. https://doi.org/10.1029/2010WR009726

Yamazaki, D., Lee, H., Alsdorf, D. E., Dutra, E., Kim, H., Kanae, S., & Oki, T. (2012). Analysis of the water level dynamics simulated by a global river model: A case study in the Amazon River. *Water Resources Research*, *48*(9). https://doi.org/10.1029/2012WR011869

Yu, D., & Lane, S. N. (2006). Urban fluvial flood modelling using a two-dimensional diffusion-wave treatment, part 1: Mesh resolution effects. *Hydrological Processes*, *20*(7), 1541–1565. https://doi.org/10.1002/hyp.5935

Zhao, G., Xu, Z., Pang, B., Tu, T., Xu, L., & Du, L. (2019). An enhanced inundation method for urban flood hazard mapping at the large catchment scale. *Journal of Hydrology*, *571*, 873–882. https://doi.org/10.1016/J.JHYDROL.2019.02.008

19447973, 2024, 5, Downloaded from https://agupubs.onlinelibrary.wiley.com/doi/10.1029/2023WR035334 by Helmholtz-Zentrum Potsdam GFZ, Wiley Online Library on [14/05/2024]. See the Terms and Conditions (https://onlinelibrary.wiley.com/terms-and-conditions) on Wiley Online Library for rules of use; OA articles are governed by the applicable Creative Commons License